The Astrophysical Journal, 977:208 (16pp), 2024 December 20 https://doi.org/10.3847/1538-4357/ad8e36

A High-resolution Far-infrared Survey to Probe Black Hole–Galaxy Co-evolution

Matteo Bonato[1], David Leisawitz[2], Gianfranco De Zotti[3], Laura Sommovigo[4], Irene Shivaei[5], C. Megan Urry[6], Duncan Farrah[7], Locke Spencer[8], Berke V. Ricketti[8], Hannah Rana[9], Susanne Aalto[10], David B. Sanders[7], and Lee G. Mundy[11]
[1] INAF—Istituto di Radioastronomia and Italian ALMA Regional Centre, Via Gobetti 101, Bologna, I-40129, Italy; matteo.bonato@inaf.it
[2] Goddard Space Flight Center, 8800 Greenbelt Rd., Greenbelt, MD 20771, USA
[3] INAF—Osservatorio Astronomico di Padova, Vicolo dell'Osservatorio 5, I-35122 Padova, Italy
[4] Center for Computational Astrophysics, Flatiron Institute, 162 5th Avenue, New York, NY 10010, USA
[5] Centro de Astrobiología (CAB), CSIC-INTA, Ctra. de Ajalvir km 4, Torrejón de Ardoz, E-28850, Madrid, Spain
[6] Yale University, P.O. Box 208120, New Haven, 06520-8120CT, USA
[7] University of Hawai'i at Mānoa, Honolulu County, Hawaii, 96822, USA
[8] University of Lethbridge, Lethbridge, Alberta, T1K 3M4, Canada
[9] Center for Astrophysics | Harvard & Smithsonian, 60 Garden Street, Cambridge, MA 02138, USA
[10] Department of Space, Earth and Environment, Chalmers University of Technology, 412 96 Göteborg, Sweden
[11] University of Maryland, College Park, MD 20742, USA
Received 2024 August 28; revised 2024 October 18; accepted 2024 November 1; published 2024 December 13

Abstract

Far-infrared (FIR) surveys are critical to probing the co-evolution of black holes and galaxies, since of the order of half the light from accreting black holes and active star formation is emitted in the rest-frame IR over $0.5 \lesssim z \lesssim 10$. For deep fields with areas of 1 deg^2 or less, like the legacy surveys GOODS, COSMOS, and CANDELS, source crowding means that subarcsecond resolution is essential. In this paper, we show with a simulation of the FIR sky that observations made with a small telescope (2 m) at low angular resolution preferentially detect the brightest galaxies, and we demonstrate the scientific value of a space mission that would offer subarcsecond resolution. We envisage a facility that would provide high-resolution imaging and spectroscopy over the wavelength range 25–400 μm, and we present predictions for an extragalactic survey covering 0.5 deg^2. Such a survey is expected to detect tens of thousands of star-forming galaxies and thousands of active galactic nuclei (AGNs), in multiple FIR lines (e.g., [C II], [O I], and [C I]) and continuum. At the longest wavelengths (200–400 μm), it would probe beyond the Epoch of Reionization, up to $z \sim 7$–8. A combination of spectral resolution, line sensitivity, and broad spectral coverage would allow us to learn about the physical conditions (temperature, density, and metallicity) characterizing the interstellar medium of galaxies over the past ∼12 billion years and to investigate galaxy–AGN co-evolution.

Unified Astronomy Thesaurus concepts: Extragalactic astronomy (506); High-redshift galaxies (734); Active galaxies (17); Infrared excess galaxies (789)

1. Introduction

Multiwavelength surveys have provided great insights into the evolution of galaxies and active galactic nuclei (AGNs) out to the Epoch of Reionization (EoR; $z \sim 6$–7; see R. Bouwens et al. 2020; B. P. Venemans et al. 2020; see also J. A. Hodge & E. da Cunha 2020 for a review of high-z submillimeter observations and, e.g., S. L. Finkelstein et al. 2023 and D. J. Eisenstein et al. 2023 for recent surveys with the James Webb Space Telescope or JWST). These objects exhibit a broad range of rest-frame spectral energy distributions (SEDs), from far-infrared (FIR) to ultraviolet energies for galaxies and from radio through gamma-ray energies for AGNs. Thus, it is vital to have broad wavelength coverage over a wide redshift range in order to reliably quantify the total energy emitted by these sources and the physical mechanisms involved. The FIR (defined here as 25–400 μm) is particularly important, because dust obscures most star-forming galaxies (SFGs; G. Lagache et al. 2005; B. C. Lemaux et al. 2014; M. Pérez-Torres et al. 2021) and AGNs (E. Treister et al. 2004; A. E. Truebenbach & J. Darling 2017; R. C. Hickox & D. M. Alexander 2018; T. T. Ananna et al. 2019; B. Laloux et al. 2023), so even though they generate most of their primary radiation in the ultraviolet, we observe reprocessed light emitted primarily at FIR wavelengths. That is, most of the detectable energy emitted from stars and black hole (BH) accretion comes out in the FIR at $z \leqslant 3$ (see P. Madau & M. Dickinson 2014). Cosmic star formation and BH accretion histories are dominated by the FIR emission coming from dusty SFGs and AGNs at $z \leqslant 3$. Without this crucial wave band, we cannot understand the energetics of AGNs, the processes of star formation, or the co-evolution of BHs and galaxies (D. Lutz 2014; E. Pouliasis et al. 2020; C. Auge et al. 2022; J. Lyu & G. Rieke 2022; J. E. Thorne et al. 2022; B. Laloux et al. 2023).

Multiwavelength surveys from the past two decades span an extensive range in luminosity and redshift, probing massive sources ($M_\star > 10^9\,M_\odot$) out to $z \sim 4$–6 (galaxies: e.g., A. L. Faisst et al. 2020; O. Le Fèvre et al. 2020; R. J. Bouwens et al. 2022; A. C. Carnall et al. 2023; and AGNs: e.g., B. P. Venemans et al. 2020; D. D. Kocevski et al. 2023; J. Scholtz et al. 2023).

Wide, shallow surveys in the mid-IR (MIR) and FIR have been done with the Wide-Field Infrared Survey Explorer (E. L. Wright et al. 2010) and the Herschel Spectral and Photometric Imaging REceiver (SPIRE; S. Eales et al. 2010;

S. J. Oliver et al. 2012; M. P. Viero et al. 2014). But the deep fields, like the Great Observatories Origins Deep Survey (GOODS, centered on the Chandra Deep Fields South and North; M. Giavalisco et al. 2004; E. Treister et al. 2004, 2006; B. D. Lehmer et al. 2012; Y. Q. Xue et al. 2012; P. Ranalli et al. 2013; T. Liu et al. 2017; B. Luo et al. 2017), the Cosmic Evolution Survey (COSMOS; N. Cappelluti et al. 2007, 2009; G. Hasinger et al. 2007; D. B. Sanders et al. 2007; N. N. Scoville et al. 2007; M. Elvis et al. 2009; F. Civano et al. 2012, 2016; V. Smolčić et al. 2017a, 2017b; I. Heywood et al. 2022; J. R. Weaver et al. 2022), the Cosmic Assembly Near-infrared Deep Extragalactic Legacy Survey (CANDELS; N. A. Grogin et al. 2011; A. M. Koekemoer et al. 2011; A. Galametz et al. 2013; Y. Guo et al. 2013; H. Nayyeri et al. 2017; M. Stefanon et al. 2017; G. Barro et al. 2019), the All-wavelength Extended Groth strip International Survey (M. Davis et al. 2007; N. P. Konidaris et al. 2007; M. Symeonidis et al. 2007; E. S. Laird et al. 2009; K. Nandra et al. 2015), the surveys of the Lockman Hole and ELAIS regions (G. Hasinger et al. 2001; M. W. Werner et al. 2004; K. Coppin et al. 2006; M. d. Polletta et al. 2006; E. A. González-Solares et al. 2011; J. C. Mauduit et al. 2012; S. J. Oliver et al. 2012; I. Prandoni et al. 2018; M. Bonato et al. 2021; R. Kondapally et al. 2021), reach flux levels where FIR-emitting sources are heavily confused at resolutions greater than a few arcseconds.

Even a large single-dish IR telescope, like the 3.5 m Herschel Space telescope, has a spatial resolution in the tens of arcseconds, hopeless for resolving individual sources in the deeper fields. Moreover, precise positions are needed to match FIR sources with their counterparts at optical and X-ray energies, as the full SED is needed to disentangle emission from starlight and from accretion. For decades, subarcsecond resolution has been available for surveys in the optical, thanks to the Hubble Space Telescope (R. E. Williams et al. 1996, 2000), and X-ray, thanks to the Chandra X-Ray Observatory (M. C. Weisskopf et al. 2000; W. N. Brandt et al. 2001), but not the FIR.

Due to the limited sensitivity and the relatively bright confusion limits of Spitzer[12] and Herschel,[13] dust-obscured star formation in typical galaxies is well constrained only up to redshifts $z \sim 2.5-3$ (N. Reddy et al. 2012; C. Gruppioni et al. 2013; P. Madau & M. Dickinson 2014; J. Álvarez-Márquez et al. 2016; I. Shivaei et al. 2017). At higher redshift, the selection bias toward the most IR-luminous and/or gravitationally lensed galaxies (M. Negrello et al. 2010, 2014, 2017; D. A. Riechers et al. 2013; Planck Collaboration XXVII 2015; I. Oteo et al. 2016; D. P. Marrone et al. 2018; J. Greenslade et al. 2020), as well as the lack of multiple FIR-band detections of large galaxy samples, casts large uncertainties on star formation rate density (SFRD) studies (see, e.g., C. Gruppioni et al. 2020; C. M. Casey et al. 2021; F. Loiacono et al. 2021; H. S. B. Algera et al. 2023; L. Barrufet et al. 2023 for the latest constraints on the dust-obscured SFRD at $z = 4-7$). Thus, our view of cosmic star formation at early epochs is still far from complete (Figure 1).

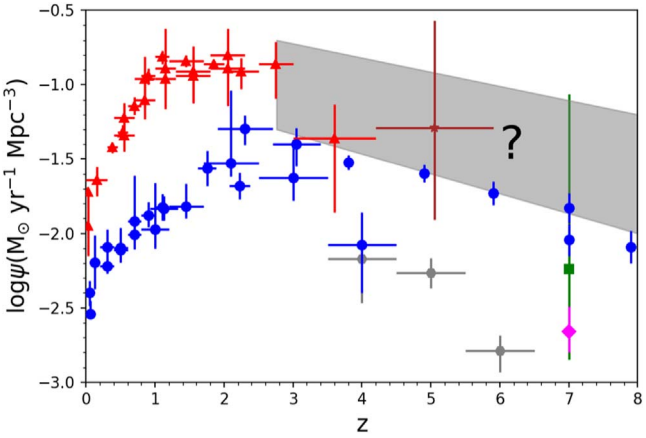

Figure 1. Evolution of the cosmic star formation history from UV data (uncorrected for dust extinction) and from FIR data (blue circles and red triangles, respectively; data taken from the P. Madau & M. Dickinson 2014 compilation). Because of dust obscuration, UV surveys miss a large fraction of the cosmic star formation, recovered by FIR data. The latter, however, is largely missing at $z \gtrsim 3$, due to the strong confusion limits affecting the Herschel SPIRE surveys. As a consequence, our understanding of the cosmic star formation history is incomplete. The reference survey described in this paper would extend measurements up to the EoR. As further examples of more recent measurements, we also plot data points from: C. M. Casey et al. (2021; gray hexagons), derived from the ALMA "MORA" survey on a sample of 2 mm selected dusty SFGs; from F. Loiacono et al. (2021; the "field" case—brown star), derived from the ALMA "ALPINE" survey on a sample of serendipitous [C II] emitters; from H. S. B. Algera et al. (2023; results based on their Monte Carlo approach—green square); and from L. Barrufet et al. (2023; magenta diamond) derived from the ALMA "REBELS" survey on a UV-selected galaxy sample.

Recent JWST observations have significantly enhanced our understanding of the unobscured SFR in galaxies out to unprecedentedly early epochs (redshift $z > 10$; see, e.g., C. M. Casey et al. 2023; C. T. Donnan et al. 2023a; S. L. Finkelstein et al. 2023; Y. Harikane et al. 2023; B. E. Robertson et al. 2023; D. J. McLeod et al. 2024). Most recent unobscured SFRD constraints derived from UV luminosity function (LF) studies with JWST show evidence of gradual evolution over the redshift range $z = 8$–13 (e.g., N. J. Adams et al. 2023; R. Bouwens et al. 2023; R. J. Bouwens et al. 2023; C. T. Donnan et al. 2023a, 2023b; Y. Harikane et al. 2023; G. C. K. Leung et al. 2023; D. J. McLeod et al. 2024). The lack of strong evolution in the bright end of the LF at $z > 12.5$ (Y. Harikane et al. 2023; B. E. Robertson et al. 2023; C. T. Donnan et al. 2024; D. J. McLeod et al. 2024) has led to suggestions that galaxies at such early epochs might experience increased star formation efficiencies (e.g., Y. Harikane et al. 2023; L. Y. A. Yung et al. 2023), possibly due to the lack of feedback (A. Dekel et al. 2023). However, more recent constraints at $z = 12$–14.5 (C. T. Donnan et al. 2024) seem to be consistent with theoretical predictions (from analytical models—A. Ferrara et al. 2023; semi-analytical models—V. Mauerhofer & P. Dayal 2023; and simulations—FLARES; M. R. Lovell et al. 2020; A. Vijayan et al. 2020; S. M. Wilkins et al. 2023), without requiring major evolution in dust content and/or star formation efficiencies of massive and early galaxies.

It is important to recognize that JWST's selection of rest-frame UV-bright objects introduces a bias in our view of the

[12] The Spitzer InfraRed Array Camera (IRAC) 5σ point-source sensitivity for a 200 s exposure time in low background is 2.0, 4.2, 27.5, and 34.5 μJy for the 3.6, 4.5, 5.8, and 8.0 μm channels, respectively (IRAC Instrument Handbook; https://irsa.ipac.caltech.edu/data/SPITZER/docs/irac/iracinstrumenthandbook/IRAC_Instrument_Handbook.pdf). The 5σ confusion limits for the Multiband Imaging Photometer for Spitzer were estimated by H. Dole et al. (2004) to be 56 μJy, 3.2 mJy, and 40 mJy at 24, 70, and 160 μm, respectively.

[13] The 5σ confusion limits of Herschel PACS are 0.4 mJy in the 70 μm passband (S. Berta et al. 2011) and 0.75 and 3.4 mJy at 100 and 160 μm, respectively (B. Magnelli et al. 2013). Those of SPIRE are 29, 31.5, and 34 mJy beam^{-1} at 250, 350, and 500 μm, respectively (H. T. Nguyen et al. 2010).

SFRD at $z > 4$, where previously mentioned studies (C. Gruppioni et al. 2020; C. M. Casey et al. 2021; F. Loiacono et al. 2021; H. S. B. Algera et al. 2023; L. Barrufet et al. 2023) have shown that the obscured SFR can contribute significantly to the cosmic SFR density.

In the following sections of this paper, we aim to demonstrate how a survey performed by an FIR interferometer, achieving subarcsecond resolution, can overcome these limitations and advance our understanding of galaxy–BH co-evolution.

This progress will be realized by exploring the rich array of spectral features in the FIR, which hold the key to deciphering the underlying physical processes governing galaxy and AGN evolution.

Important MIR/FIR lines can be detected at redshifts of interest, revealing properties of the interstellar medium (ISM) and the hardness of the primary radiation (C. L. Carilli & F. Walter 2013; see also D. Farrah et al. 2007, 2013 for the main MIR/FIR spectroscopic diagnostics).

Prominent polycyclic aromatic hydrocarbon (PAH) features, which contribute a significant fraction of the total IR emission and trace the SFR (J. D. T. Smith et al. 2007; D. A. Riechers et al. 2013; I. Shivaei et al. 2024), will be visible up to high redshifts (A. Li 2020). PAH features' ratios have been proposed as an indicator for detecting deeply-dust-enshrouded AGNs (I. García-Bernete et al. 2022). The rotational MIR H_2 emission lines allow us to estimate temperatures and masses of moderately warm gas (D. Rigopoulou et al. 2002).

Lines like [C II] at 157.7 μm and [O I] at 63.18 and 145.52 μm dominate the cooling of neutral gas. The [C II] line—which is also emitted by photodissociating regions (see M. G. Wolfire et al. 2022 for a recent review)—is one of the brightest FIR lines and thus has been observed in a large number of SFGs out to $z \sim 5$–8 (see, e.g., T. J. L. C. Bakx et al. 2020; M. Béthermin et al. 2020; S. Carniani et al. 2020; R. J. Bouwens et al. 2022). Gas in the ionized phase is traced by [O III] at 51.81 and 88.36 μm and by [N II] at 121.9 μm. Thus, a spectroscopic survey over the wavelength range 25 −400 μm, with complementary Atacama Large Millimeter/submillimeter Array (ALMA) observations at longer wavelengths, can disentangle the contributions of the various ISM phases to redshifts stretching back to the EoR.

Lines with high ionization potential, like [O IV] at 25.89 μm, are excited by hard UV emission and thus trace AGN activity (e.g., E. Sturm et al. 2002). Because the line intensity is linearly correlated with AGN luminosity (M. Meléndez et al. 2008; M. Bonato et al. 2014a), it provides an extinction-free measure of the accretion rate.

Other important AGN tracers are [Ne V] lines at 14.32 and 24.31 μm (ionization potential of $\simeq$100 eV; S. Tommasin et al. 2010), and their ratio is a measure of the electron density in highly ionized regions (E. Sturm et al. 2002; S. Tommasin et al. 2010). The simultaneous detection of lines that trace the star formation and the accretion rates will allow testing of galaxy–AGN co-evolution.

An illustrative subsample of the brightest redshifted spectral lines in the 25–400 μm FIR spectral window, used for the predictions provided in this paper, is listed in Table 1.

The structure of the paper is as follows. Section 2 describes simulations demonstrating the importance of high resolution for beating the confusion noise, obtaining sensitive measurements of individual galaxy spectra, and exploiting emission lines to characterize physical conditions of galaxies. Section 3 describes a case study for a reference FIR survey. It details the physically grounded model used for our calculations and presents the related achievable results. Our results are discussed in Section 4. The main conclusions from our analysis are summarized in Section 5.

Calculations are carried out adopting a standard flat ΛCDM cosmology, with $\Omega_m = 0.31$, $\Omega_\Lambda = 0.69$, and $h = H_0/100\,\mathrm{km\,s^{-1}\,Mpc^{-1}} = 0.677$ (Planck Collaboration VI 2020).

Table 1
Bright Spectral Lines Used in This Paper

Species	Wavelength (μm)
Photodissociation Region	
PAH	3.3, 6.2, 7.7, 8.6, 11.3, 12.7
H_2	6.91, 9.66, 12.28, 17.03
[Cl II]	14.38
[Fe II]	25.98
[S III]	33.48
[Si II]	34.82
[O I]	63.18, 145.52
[C II]	157.7
[C I]	370.42
Stellar/H II Regions	
[Ar II]	6.98
[Ar III]	8.99, 21.82
[SI V]	10.49
H I	12.37
[Ne II]	12.81
[Ne III]	15.55
[Fe II]	17.93
[S III]	18.71
[Fe III]	22.90
[O III]	51.81, 88.36
[N III]	57.32
[N II]	121.90, 205.18
AGNs	
[Ne VI]	7.63
[Ar V]	7.90, 13.09
[Mg V]	13.50
[Ne V]	14.32, 24.31
[O IV]	25.89
Coronal Regions	
[Si VII]	6.50
[Ca V]	11.48

Note. In this table, the four classes into which the spectral lines are subdivided correspond to the regions where they are mainly produced. Note that some lines can be observed in multiple regions, albeit with varying intensities. For the subdivision of most of the lines, we followed the L. Spinoglio et al. (2012) critical density for collisional de-excitation versus ionization potential diagnostics (their Figure 4).

2. Probing Beyond the Confusion Noise Floor

Spatial confusion is an impediment to scientific information retrieval, but how limiting is this effect? A cold (~4 K) FIR telescope equipped with state-of-the-art detectors theoretically could be limited in sensitivity only by photon noise from the natural sky background. However, a 3.5 m telescope like Herschel barely resolves point sources separated by 7″ at 100 μm, and already at flux densities well above the achievable sensitivity galaxies are much more closely spaced. For

Herschel, the rms confusion noise floor was 5.8, 6.3, and 6.8 mJy beam^{-1} at 250, 350, and 500 μm, respectively (H. T. Nguyen et al. 2010). Herschel SPIRE was used to measure galaxy number counts at these wavelengths down to tens of millijanskys (D. L. Clements et al. 2010; S. J. Oliver et al. 2010). A 3.5 m or smaller telescope might survey the entire sky to the confusion limit and yet provide limited information on individual distant galaxies and galaxy evolution. In this section, we use a model of the FIR sky at high resolution to assess the information lost due to spatial confusion. For the sake of illustration, we compare the spectra of individual simulated galaxies with one predicted to be seen with a cold 2 m telescope.

We updated the previously unpublished code designed to simulate the FIR sky at high angular resolution. The code uses the best available foreground models and generates synthetic extragalactic sources in a manner consistent with Herschel and other available measurements. To account for the FIR foregrounds, our code uses the COBE zodiacal emission model (T. Kelsall et al. 1998), IRAS measurements of the spatial distribution of Galactic cirrus (D. J. Schlegel et al. 1998), a parametric model of the cirrus spectrum (V. Zubko et al. 2004), and a power law with index −2.5 fitted to cirrus spatial structure seen with IRAS on arcminute and coarser scales to extrapolate the structure to never-before-seen subarcsecond scales. This foreground model estimates the specific intensity of the FIR emission as a function of sky coordinates, solar elongation angle, and wavelength.

Star-forming disk galaxies are added to the foreground emission. Empirical full-sky galaxy counts binned by flux density, wavelength, and redshift based on Herschel observations (M. Bonato et al. 2014a) are used as a three-dimensional probability distribution function to assign random flux density and redshift values to the individual galaxies for a chosen wavelength. Initial sky coordinates and orientation parameters are also chosen at random, and we adjust the initial coordinates to allow for stable clustering (P. J. E. Peebles 1980). The number of simulated galaxies is determined by the modeled field size and a 1 μJy flux limit. Each galaxy has a J. L. Sérsic (1968) brightness profile with $m = 1$ (L. Ciotti & G. Bertin 1999) and a disk half-light radius R_e based on its luminosity and redshift. The latter relationship is derived from relations between the effective radius and stellar mass (S. Shen et al. 2003), SFR and stellar mass (Y.-j. Peng et al. 2010), and the star formation–$L_{\rm IR}$ relation from M. S. Clemens et al. (2013). The size evolution at $z < 1.5$ is based on the findings of A. van der Wel et al. (2014), and galaxies at $z \geqslant 1.5$ are assumed to follow the same relationship between R_e and $L_{\rm IR}$ as those at $z = 1.5$. The model does not account for radiative transfer effects but is sufficiently realistic for the purpose at hand.

An unresolved active nucleus (AGN) lies at the center of each simulated galaxy. Its luminosity and type are assigned probabilistically, based on the galaxy's spatially and spectrally integrated IR luminosity $L_{\rm IR}$ (R. V. Vasudevan & A. C. Fabian 2007; Z.-Y. Cai et al. 2013; C.-T. J. Chen et al. 2013; M. Bonato et al. 2014a). The ratio of Type 1 to Type 2 AGNs is based on S. Bianchi et al. (2012), with reference to data from G. Hasinger (2008). The AGN-to-star-formation ratio varies from galaxy to galaxy, according to the relation between star formation and accretion rate derived by C.-T. J. Chen et al. (2013), allowing for the observed dispersion.

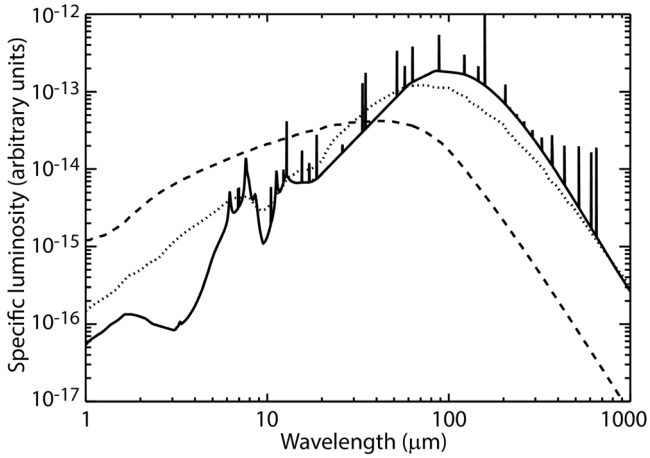

Figure 2. The same rest-frame spectra are adopted for all galaxies and AGNs. The solid curve is the spectrum of a star-forming disk galaxy. The dotted curve is the adopted SED of a Type 2 AGN, and the dashed curve is the SED of a Type 1 AGN. The spectral templates are normalized such that the 8–1000 μm IR luminosity is 1 erg s^{-1}. Each galaxy's spectrum is scaled to its actual luminosity. These SEDs are taken from Z.-Y. Cai et al. (2013).

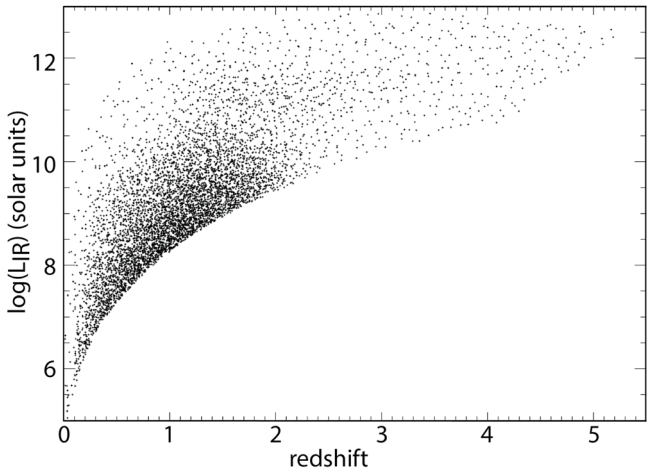

Figure 3. Total IR luminosities (sum of star-forming disk and AGN components) and redshifts of 6275 galaxies in the simulated COSMOS field area. The lower envelope corresponds to the fact that source counts were modeled to a 1 μJy lower bound in flux density.

Rest-frame spectra are adopted for the disk emission and for each of the two AGN types (Z.-Y. Cai et al. 2013; M. Bonato et al. 2019). In a step toward simplicity, we use the same rest-frame template spectra for all galaxies and AGNs, and we model only the SEDs of AGNs, ignoring their line emission (Figure 2). Thus, evolutionary effects and, e.g., the effects of SFR on a galaxy's emission will not be seen in the simulated galaxy spectra.

We modeled a $4\farcm74 \times 4\farcm74$ field at the Galactic coordinates $(l,\ b) = 236\fdg822,\ 42\fdg1216$, chosen for its location in the COSMOS deep field (N. Scoville et al. 2007). The simulated field was assumed to be observed at a solar elongation angle of 160°, which affects the zodiacal emission brightness. Figure 3 shows the redshifts and derived luminosities of the 6275 galaxies in the simulated field. The mean separation between nearest neighbors is approximately $1\farcs8$.

We calculated model maps of specific intensity at wavelengths ranging from 25 to 400 μm in 0.05 μm increments at wavelengths $\leqslant$100 μm and 0.5 μm increments at longer

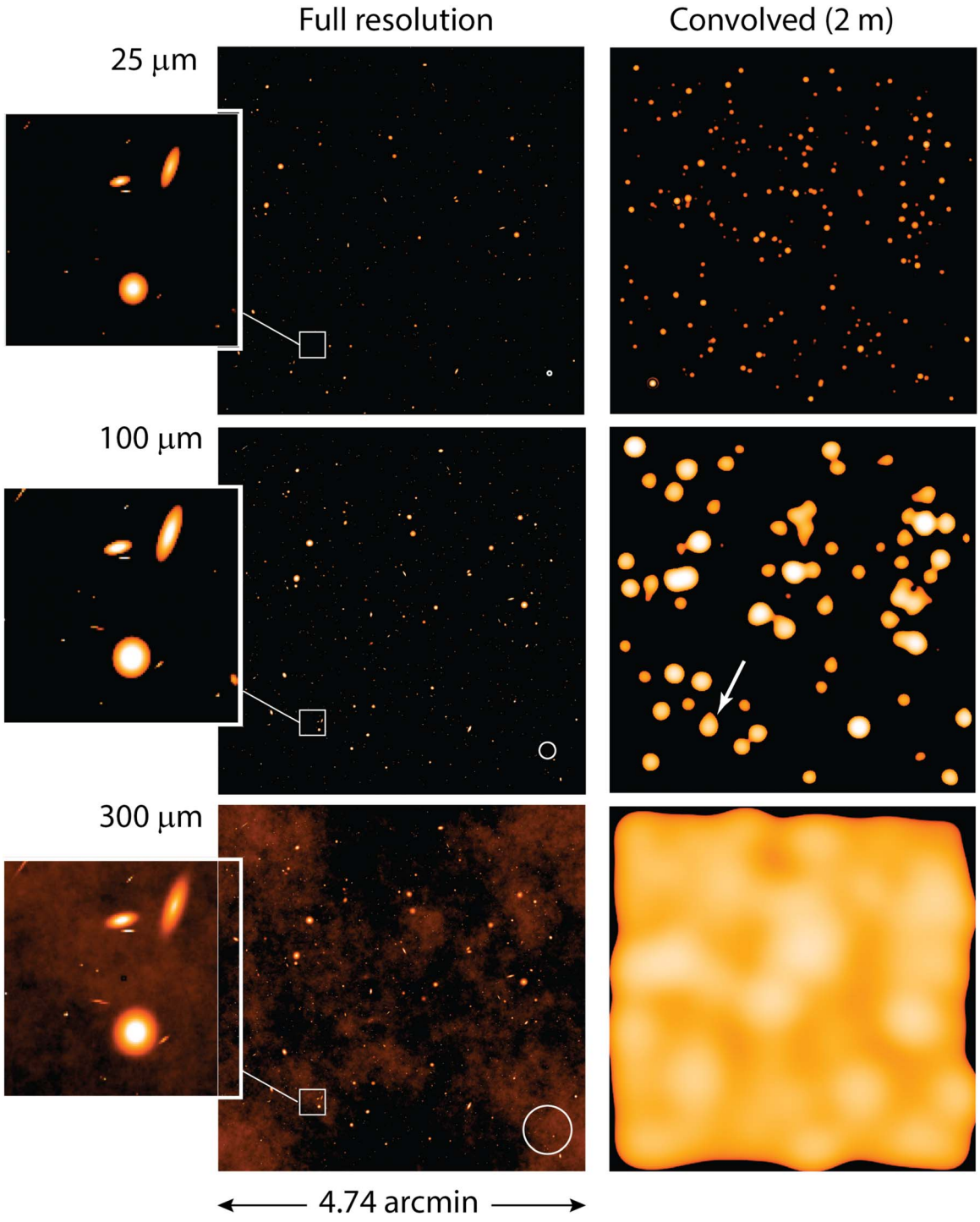

Figure 4. 25, 100, and 300 μm wavelength slices from the simulated hyperspectral data cube (left, with insets that reveal the richness of the model data set) and convolved to the resolution of a 2 m telescope (right). The beam size of a 2 m telescope at each wavelength is shown with a circle, indicating that light from most or all the galaxies in the inset area would blend at 100 μm and longer wavelengths. The white arrow in the 100 μm convolved image points to the location of the aperture analyzed in the spectral domain.

wavelengths. Collectively, the synthesized images comprise a hyperspectral data cube with 2101 wavelength slices. Each image has 8192^2 pixels at $0\farcs0347$ pixel^{-1}, enabling convolution to the resolution of an interferometer or a single-aperture telescope. The spectral lines are smoothed to $\Delta\lambda = \lambda(\mu\mathrm{m})/300$ wavelength channels to derive the equivalent flux densities.

Figure 4 shows 25, 100, and 300 μm slices from the simulated data cube and corresponding images convolved to the resolution of a notional 2 m diameter diffraction-limited telescope with a 20 cm central obscuration. Each image is shown on a logarithmic intensity scale, with minima close to the foreground intensities at each wavelength and maxima of 50 MJy sr^{-1} in all the full-resolution maps and 50, 10, and 5 MJy sr^{-1} in the convolved maps at 25, 100, and 300 μm, respectively. Cirrus emission is noticeable in the 300 μm full-resolution image. We ignore photon shot noise. Due to beam

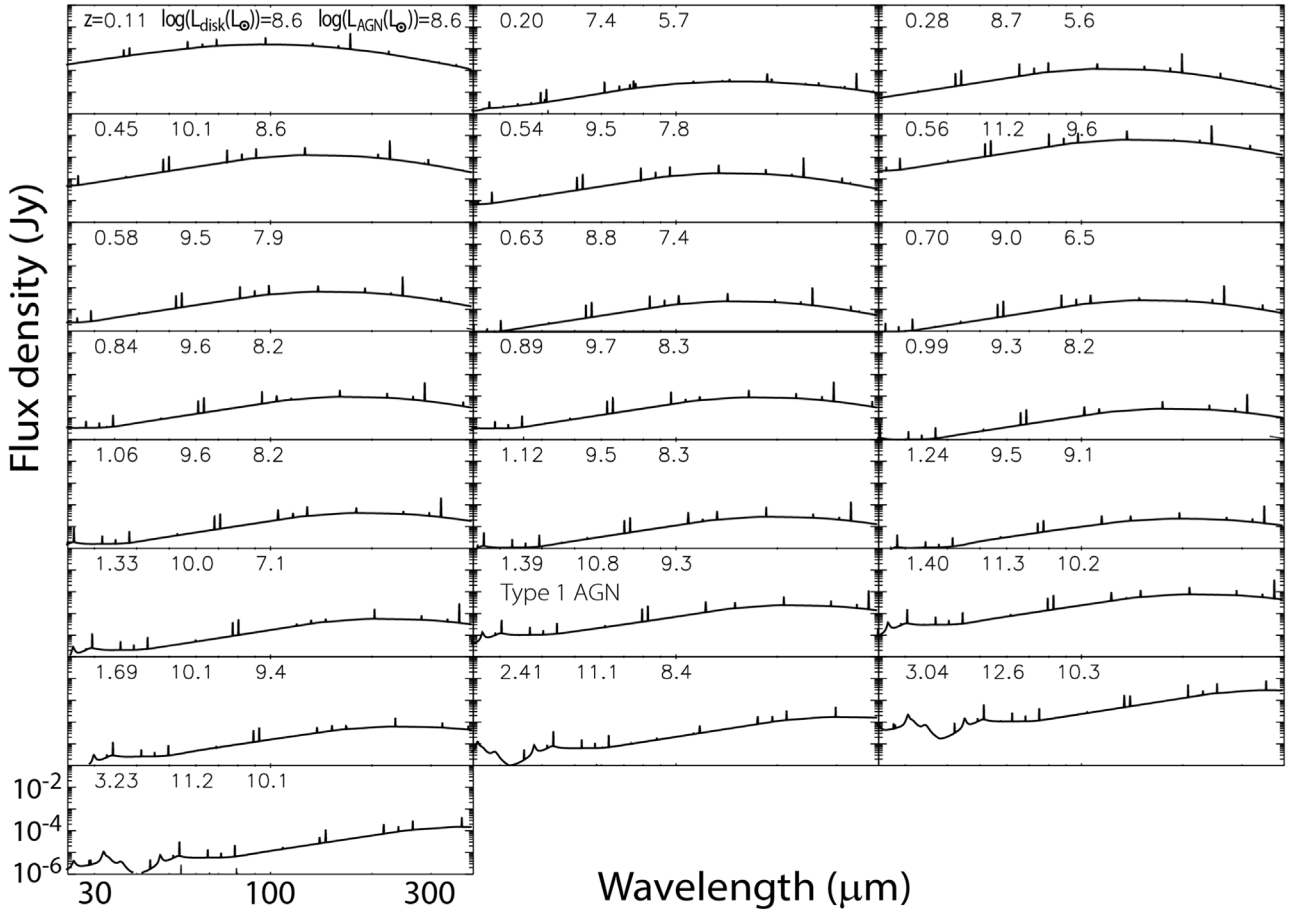

Figure 5. Spatially integrated spectra of the 22 brightest of 48 simulated galaxies in the analyzed aperture area, shown in order of increasing redshift in raster fashion from top left to bottom right. The remaining galaxies are at best barely brighter than 10 μJy. The same foreground spectrum was subtracted from each galaxy's spectrum. The foreground spectrum is extracted from the data cube at the location of the darkest pixel at 25 μm. The three numbers in each panel indicate the galaxy's redshift, the base-10 logarithm of its disk-integrated IR (8–1000 μm) luminosity in solar units, and the galaxy's AGN luminosity in the same units, respectively. Only one bright galaxy, as indicated, has a Type 1 AGN, while all the others have Type 2 AGNs. The galaxy at redshift $z = 3.04$ is the only one in the aperture area with a luminosity greater than $10^{12}\,L_{\odot}$ and would be considered "ultraluminous."

dilution, the faintest galaxies are not visible above the foreground emission in the 2 m telescope images, even at 25 μm where confusion is negligible.

We probe the spectral domain to understand more fully the effects of confusion, choosing for analysis an aperture centered on the amorphous bright spot at the tip of the white arrow in Figure 4. The aperture area corresponds to the 100 μm Airy disk of a 2 m telescope—$2.44\lambda/d$—and the same aperture was used at all wavelengths. 48 simulated galaxies lie within the aperture. The spectra of 22 of these galaxies—those with significant emission greater than 10 μJy—are shown in Figure 5. Two of the 48 galaxies host a Type 1 AGN; the rest are of Type 2. None of the AGNs outshine their host galaxies, whereas that happens in a handful of cases in the overall sample of 6275 simulated galaxies. If they could be measured, each of these spectra would have a story to tell about the galaxies' physical conditions, metallicity, and importance of the AGN, as well as the redshift. Collectively, such spectra would inform our understanding of galaxy evolution and the co-evolution of the galaxies and their central supermassive BHs (SMBHs). An observatory offering subarcsecond angular resolution could measure the FIR spectra of thousands of galaxies in a field the size of that shown in Figure 4. Several fields could be observed to allow for cosmic variance.

What would an on-axis 2 m diameter telescope see? To answer that question, we integrate spatially over the pixels in the same aperture area as that described above, but derive the spectrum from convolved images like those shown on the right-hand side of Figure 4. The spectrum derived from the convolved images is shown in the lower curve in Figure 6(a). Because even the darkest pixel in the 25 μm convolved map contains significant extragalactic source emission, a model is needed to subtract the foreground spectrum. Here, we are fortunate to know the computed foreground, but an observer who encounters confusion noise will only have an estimate, leaving room for systematic error in the foreground subtraction. Uncertainty in the foreground could affect the continuum shape in the aperture-integrated spectrum.

For comparison with the spectrum derived from the convolved maps, the upper curve in Figure 6(a) shows the sum of the spectra of all the individual galaxies in the aperture area (multiplied by a factor of 3 to produce an offset for clarity). Panels (b) and (c) of Figure 6 show the difference between the convolved map spectrum and the summed galaxy spectra and indicate that both the continuum and line emission seen in the convolved maps are not a simple mixture of the spectra of the individual galaxies. Line emission can be underestimated or overestimated. The shape of the continuum seen with a 2 m telescope is not simply the sum of the continua

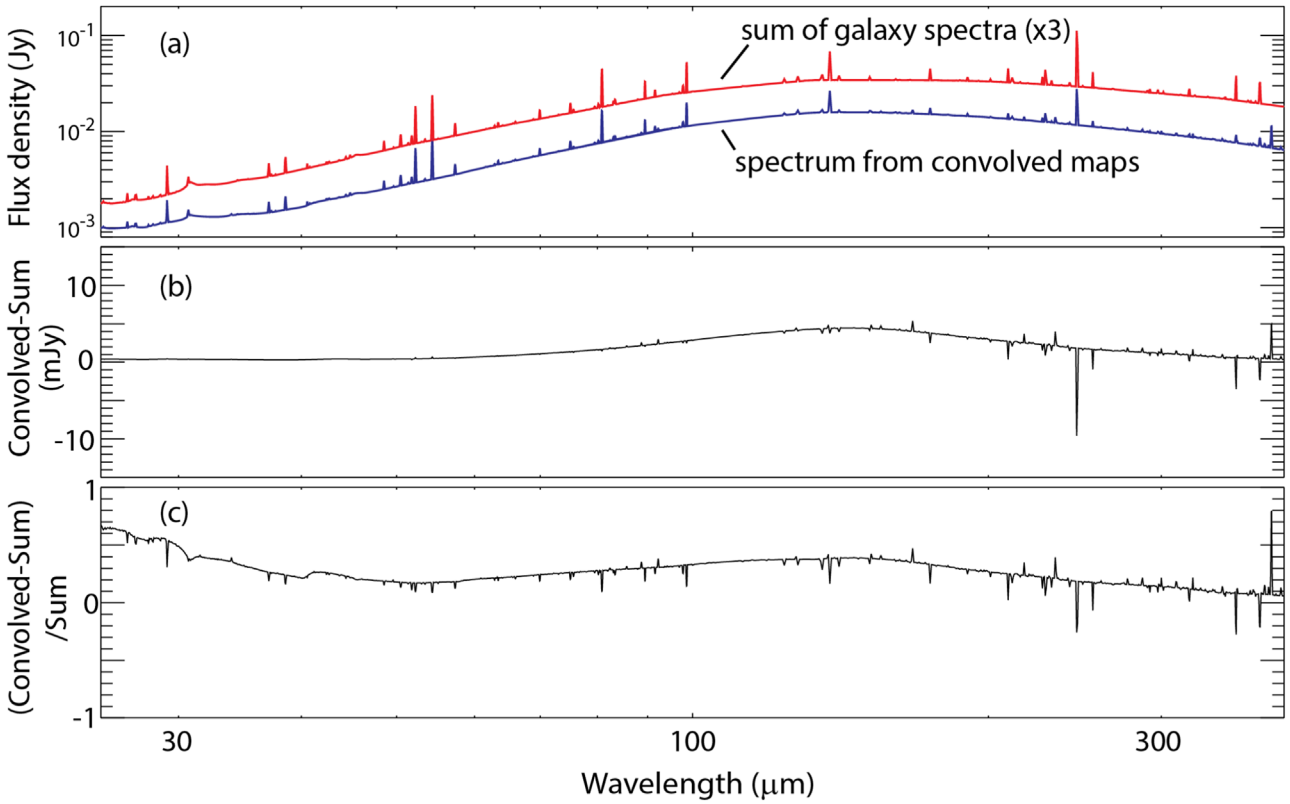

Figure 6. (a) Blue: spectrum extracted from the convolved maps integrated over the same aperture area as that containing 48 galaxies—from which the spectra of the brightest sources are shown in Figure 5—with the "known" model foreground emission subtracted. Red: the summed spectrum of all 48 galaxies in the aperture multiplied by a factor of 3 to offset the resulting spectrum from the lower curve. Six galaxies—those at redshifts 0.11, 0.45, 0.56, 1.39, 1.40, and 3.04—contribute significantly to the emission seen in the summed spectrum, and a single galaxy at $z = 0.56$ dominates. The PAH feature seen at ∼30 μm is primarily attributable to the ultraluminous galaxy at $z = 3.04$. (b) The difference between the convolved spectrum (lower/blue curve in (a)) and the sum of the galaxy spectra in the analyzed aperture (upper/red curve in (a)). (c) The corresponding fractional difference between the two spectra. Spectral line blending is most severe at the long-wavelength end of the spectrum, due to the larger beam size at longer wavelengths. Line intensities can be either underestimated or overestimated in a spectrum obtained with a 2 m telescope. At wavelengths $\gtrsim$70 μm, the shape of the continuum is distorted, suggesting that efforts to ascribe continuum emission to individual galaxies are subject to bias from sources outside the aperture area. While not apparent in (b), the fractional difference in (c) shows that broadband PAH features from high-redshift galaxies merge at wavelengths $\lesssim$50 μm.

of the blended galaxies, because the telescope's beam size is wavelength-dependent. If we had analyzed a larger aperture area, we would have found smaller differences, but then the emission from a greater number of galaxies would be blended.

Sophisticated retrieval techniques can be used to probe below the classical confusion noise floor by a factor of ∼3 (P. D. Hurley et al. 2017; J. M. S. Donnellan et al. 2024), and it is possible to derive the redshifts of the bright galaxies that dominate the spectrum seen with a 2 m telescope. However, blending in the spectral domain and the lack of information about each galaxy's continuum emission compromise the derivation of line intensities. As described in Section 1, a great deal of information—such as information about metallicity, physical conditions in the ISM, and the presence or absence of a significant AGN—is contained in FIR spectral lines and their intensity ratios. Without accurate line intensities, much of this information would be lost or plagued with systematic uncertainty.

The convolved map spectrum differs from the sum of the spectra of the 48 galaxies in the aperture area chosen for analysis, because the beam of a 2 m telescope encompasses emission outside the 100 μm Airy disk at longer wavelengths. We find significant spectrally complex differences between the two spectra shown in Figure 6(a), illustrating the extent to which information in the spectral domain is lost or skewed as a consequence of spatial blending.

To ensure that these results are not anomalous, we repeated the analysis for another aperture centered on a different, somewhat less isolated bright spot in the convolved 100 μm image. The results were qualitatively similar to those shown in Figure 6.

Six galaxies dominate the spectrum shown in the lower curve in Figure 6(a). These galaxies lie in the redshift range 0.11–3.04 and half of them would be classified as luminous IR galaxies (LIRGs) with $L_{\rm IR} > 10^{11}\,L_{\odot}$. Similar results were found in the second analyzed aperture. This population is not representative of the general galaxy population.

With sufficient spectral resolution, one could discern the presence of multiple bright galaxies in a 2 m telescope's beam, count those galaxies, and measure their redshifts, but many faint galaxies would be overlooked. A model could be used to estimate how much continuum emission to assign to each discernible galaxy as a function of wavelength, and such a model could allow for the possible evolution in galaxy luminosity, dependence on the SFR and dust filling fraction, and metallicity, etc.—all unknown and, indeed, some of the parameters one would like to measure. However, assigning a portion of the continuum to each of the contributing galaxies is fraught with uncertainties and potential model degeneracies. At

best, one might find a self-consistent solution and have little insight into systematic errors.

To probe the co-evolution of galaxies and their central SMBHs and learn how galaxies formed and built up heavy elements and dust over cosmic time—major goals of the Astro2020 Decadal Survey (National Academies of Sciences, Engineering, & Medicine 2021)—we need sensitive far-IR spectroscopic observations of galaxies out to high redshifts. We must characterize physical conditions, such as the hardness of the interstellar radiation field, measure metallicity, and test hypotheses for how these galaxy characteristics change as a function of redshift. FIR spectral line strength ratios, PAH features, and the continuum shape all contain the desired information. Thus, direct measurements of individual galaxy spectra are far superior probes of evolution. Such measurements are possible with an observatory that offers subarcsecond resolution, spectral resolving power in the hundreds to thousands, and sensitivity of the order of microjanskys.

3. Probing Galaxy–AGN Co-evolution with a High-resolution FIR Survey

As mentioned in Section 1, subarcsecond resolution is attainable at FIR wavelengths with interferometry. Given the significant advancements in FIR interferometry technology, a large-scale space mission in the next decade is highly feasible. Such a mission could provide invaluable insights into the co-evolution of galaxies and BHs. To demonstrate the potential of such a mission and to benchmark a notional high-resolution FIR sky survey (hereafter, the "reference survey"), we consider the measurement capabilities of the Space Infrared Interferometric Telescope (SPIRIT; D. Leisawitz et al. 2007, 2008; D. Leisawitz & SPIRIT Origins Probe Mission Concept Study Team 2009), which can achieve the JWST-like resolution essential for studying the co-evolution of galaxies and accreting BHs. Referring to Table 3 of D. Leisawitz & SPIRIT Origins Probe Mission Concept Study Team (2009), SPIRIT has a wavelength range of 25–400 μm, an instantaneous field of view (FoV) of 1′, and an angular resolution 0.3 ($\lambda/100\,\mu$m) arcsec. The point-source continuum sensitivities (5σ; 24 hr per FoV) are 14, 20, 31, and 48 μJy, at 35, 70, 140, and 280 μm, respectively. The instrument design provides, in addition to spatial interferometry, Fourier transform spectroscopy with spectral resolution $R = 3175$, 5058, 4265, and 3000 and spectral line detection limits of 2.9, 1.7, 1.4, and 1.3×10^{-19} W m^{-2}, respectively, at the four wavelengths and under the conditions mentioned above. The spectral resolution comes from scanning an optical delay line and it is given by the number of detectable fringes above some noise threshold. Because a moderate spectral resolution of ∼500 is enough for the purposes discussed in this paper, we would Fourier transform the full interferogram to obtain a high-R spectrum and rebin the spectral channels, gaining a factor $\sim(R/500)^{1/2}$ in sensitivity.

Figure 7 shows that such an FIR interferometer would fill the gap in our view of the cosmic star formation history mentioned in Section 1 and shown in Figure 1. It would allow us to investigate the evolution of the dust temperature (or, more directly, the SED peak temperature that is largely unconstrained at $z > 2$; L. Sommovigo et al. 2022) with cosmic time, which needs to be matched by evolutionary models.

On the spectroscopic side, the wavelength gap between JWST and ALMA translates into gaps in the redshift ranges over which MIR/FIR lines can be detected, as illustrated by Figure 8. This limits the possibility of exploiting the emission lines to study the properties of the ISM (density, temperature, and ionization state) and to investigate gas heating and cooling processes and the hardness of the radiation field linked to the presence of AGNs (see C. L. Carilli & F. Walter 2013 for a review). Such an FIR interferometer would be a valuable complement of ALMA and JWST.

This section describes the science achievable for a reference extragalactic survey covering half a square degree in 1000 hr (including overheads, ∼900 hr on sources), with predictions for the numbers of galaxies and AGNs detected in the continuum and in the main emission lines. The reference survey will achieve 5σ point-source detection limits of (8.0, 3.7, 3.3, 3.7) $\times 10^{-19}$ W m^{-2} in spectroscopy and (0.10, 0.14, 0.21, 0.33) mJy in the continuum, for the 25–50, 50–100, 100–200, and 200–400 μm wavelength intervals, respectively. This survey will detect emission from dust heated by young stars in galaxies at redshifts of up to $z \sim 7$, or even higher if the typical dust temperature continues to increase with redshift (R. Bouwens et al. 2020; L. Sommovigo et al. 2022; H. S. B. Algera et al. 2024)—which the survey will determine. The attained angular resolution will allow us to reveal the evolving structure of dusty SFGs, which reflect the physical processes that drove the galaxy buildup, such as mergers, interactions, accretion flows, the shrinking of the star formation region by dissipation, or morphological transformations.

The reference survey angular resolution at 30 μm (0.″09) corresponds, for the adopted cosmology, to linear sizes $\leqslant$0.78 kpc at $z > 1$. The available information on the size of the dusty star-forming regions (or FIR sizes) in moderate-to-high-redshift massive galaxies is still limited. W. Rujopakarn et al. (2011) found a median diameter of 4.4 kpc for a sample of LIRGs/ultraluminous IR galaxies and submillimeter galaxies (SMGs) at $0.4 < z < 2.7$, while B. Gullberg et al. (2019) derived a typical effective radius at 870 μm of $\simeq 0.''15 \pm 0.''05$ for a sample of 153 bright SMGs with a quartile range in redshift of 2.5–3.5. K.-i. Tadaki et al. (2020) reported a broad range of FIR effective radii (0.4 kpc $< R_e <$ 6 kpc) for massive SFGs at $1.9 < z < 2.6$. Similar results can also be found in J. M. Simpson et al. (2015), G. Barro et al. (2016), J. M. Simpson et al. (2017), J. A. Hodge et al. (2019), P. Lang et al. (2019), W. Rujopakarn et al. (2019), L. Pantoni et al. (2021), and in the review by J. A. Hodge & E. da Cunha (2020). At higher redshift, J. McKinney et al. (2023) provide an upper limit of 0.″44, in ALMA Band 6, for the effective radius of an FIR-luminous dusty galaxy at $z \sim 5$.

The stretching of images by gravitational lensing will make it possible to extend the morphological analysis to longer wavelengths for a sizable subset of detections. The proposed survey will shed light on this debated issue, namely the sizes of star-forming regions in distant galaxies, and on the origin of the galaxies' morphological diversity.

3.1. Model

For the predictions provided in this section, we use a more sophisticated modeling approach than that used in Section 2, where only three reference SEDs for the evolution of galaxies/AGN populations were considered. We adopt an updated version of the physically grounded analytical model by Z.-Y. Cai et al. (2013), describing the evolution of eight different populations of galaxies/AGNs. The model predicts the co-evolution of

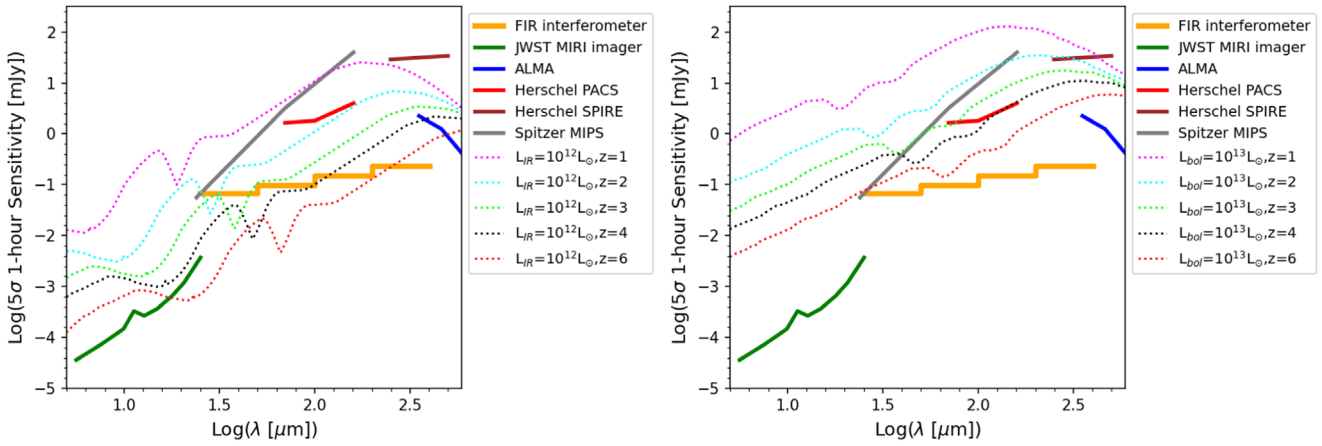

Figure 7. Template SEDs of dusty proto-spheroids with $L_{\rm IR} = 10^{12}\,L_\odot$ (left) and obscured AGNs with bolometric luminosity $L_{\rm bol} = 10^{13}\,L_\odot$ (right), at $z = 1$, 2, 3, 4, and 6, from Z.-Y. Cai et al. (2013), compared with the 5σ detection limits for 1 hr exposures of the FIR interferometer, of JWST MIRI, of the Spitzer Multiband Imaging Photometer for Spitzer, of Herschel PACS and SPIRE, and of ALMA. The luminosity of $10^{12}\,L_\odot$ corresponds to an SFR of $\simeq$100 $M_\odot$ yr^{-1}, typical of SFGs at cosmic noon ($z \simeq 2$–3).

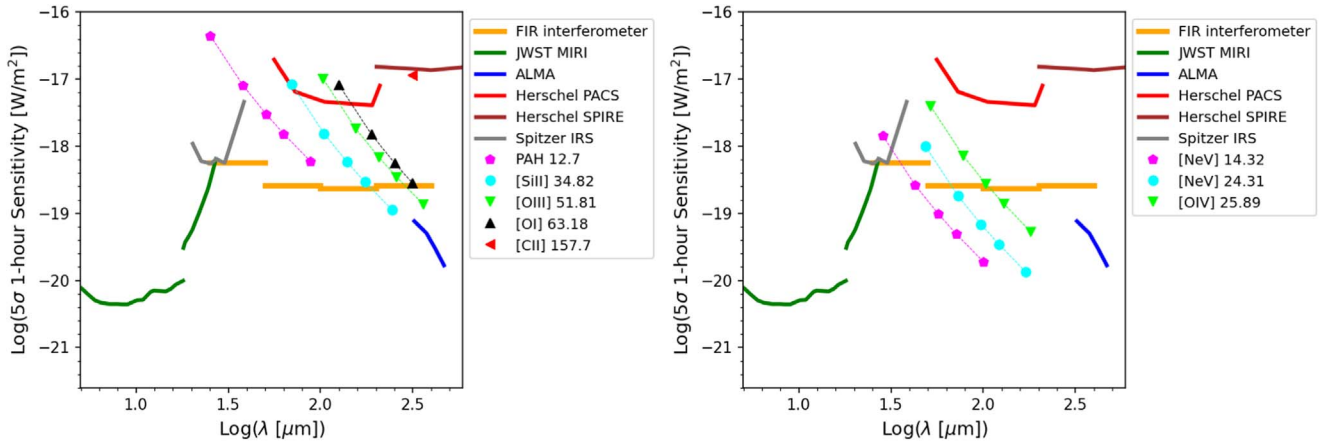

Figure 8. The predicted intensities of key spectral lines, compared to 5σ detection limits for 1 hr exposures with the FIR interferometer, JWST MIRI, Spitzer IRS, Herschel PACS and SPIRE, and ALMA. Left: lines powered by star formation from galaxies with $L_{\rm IR} = 10^{13}\,L_\odot$ at $z = 1$, 2, 3, 4, and 6 (filled symbols connected by solid lines, from left to right). Right: lines powered by AGNs with bolometric luminosity $L_{\rm bol} = 10^{14}\,L_\odot$ at the same redshifts.

spheroidal galaxies and of the associated AGNs as a function of galactic age, halo mass, and redshift. The histories of the galaxy and AGN bolometric luminosities are computed by solving a set of equations describing the evolution of three gas phases. The hot gas, initially at the virial temperature, cools and falls toward the galaxy center; the cold gas condenses into stars; the third phase consists of gas gathered around the SMBH and accreting onto it at a rate regulated by viscous dissipation of the angular momentum. The equations include recipes for supernova and AGN feedback. The model yields, at each galactic age, the bolometric luminosity of the AGN and of the host galaxy, given the halo mass and the galaxy formation redshift. The luminosity at any frequency is derived using appropriate SEDs for the galaxy and the AGN. Z.-Y. Cai et al. (2013) also computed the gravitational amplification distribution, i.e., the probability for a galaxy at redshift z to have its flux density amplified by a factor μ, as well as the clustering properties of galaxies exploiting the Halo Occupation Distribution formalism by Z. Zheng et al. (2005).

The stellar populations of present-day spheroidal galaxies and galactic bulges are relatively old, implying that they mostly formed at $z \gtrsim 1.5$. According to the model, star-forming spheroids (proto-spheroids) were the dominant contributors to cosmic star formation at high redshifts. Below $z \sim 1.5$, star formation happens primarily in starburst and late-type "normal" galaxies. The model attributes different SEDs and different evolutionary properties to the two galaxy classes. Starburst galaxies contain warmer dust and evolve faster than "normal" galaxies. In both cases, phenomenological evolutionary laws are adopted. At variance with the model for spheroids, which co-evolves the stellar and AGN components, AGNs associated with starburst and late-type galaxies were treated by Z.-Y. Cai et al. (2013) as an independent population.

A tabulation of the adopted SEDs, of counts, and of LFs at many frequencies is available at the website http://staff.ustc.edu.cn/~zcai/galaxy_agn/index.html, where extensive comparisons of model predictions with multifrequency data at several redshifts are also presented. Although relatively old, the model is still highly competitive (see, e.g., C.-C. Chen et al. 2022 and B. A. Ward et al. 2022).

In previous work, we upgraded the original phenomenological model in several ways (M. Bonato et al. 2014a). We linked the BH accretion rate (BHAR), hence the AGN bolometric luminosity, to the SFR, hence to the IR luminosity, so that the global emission of the galaxy, including the AGN contribution, is treated self-consistently. We extended the study

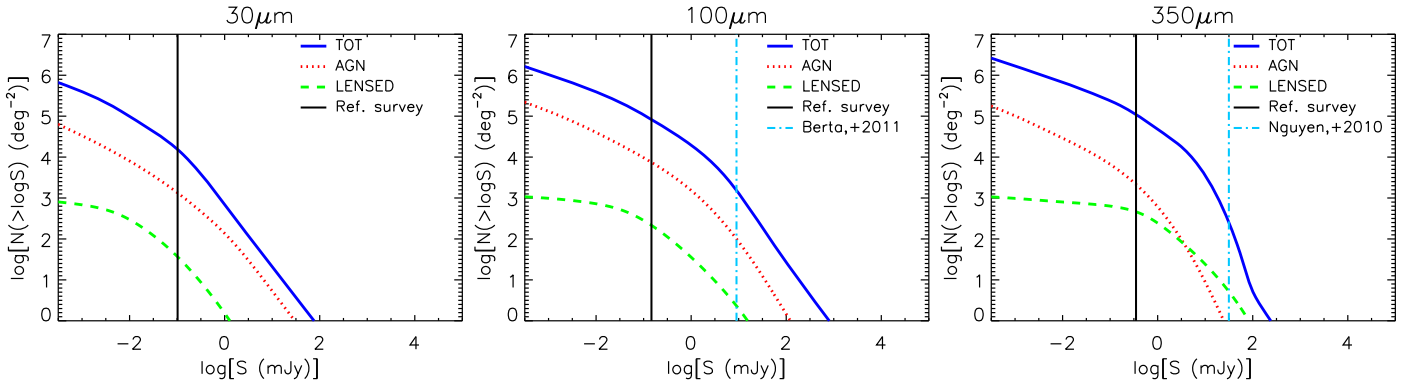

Figure 9. Integral counts per square degree at 30, 100, and 350 μm (from left to right) predicted by our model. The vertical black lines correspond to the 5σ reference survey detection limits of 0.14, 0.21, and 0.33 mJy, respectively. The vertical dotted–dashed cyan lines show, at 100 μm, the 80% completeness limit (9 mJy) of the Herschel PACS PEP survey of the COSMOS field (S. Berta et al. 2011) and, at 350 μm, the Herschel SPIRE 5σ confusion noise (31.5 mJy; H. T. Nguyen et al. 2010).

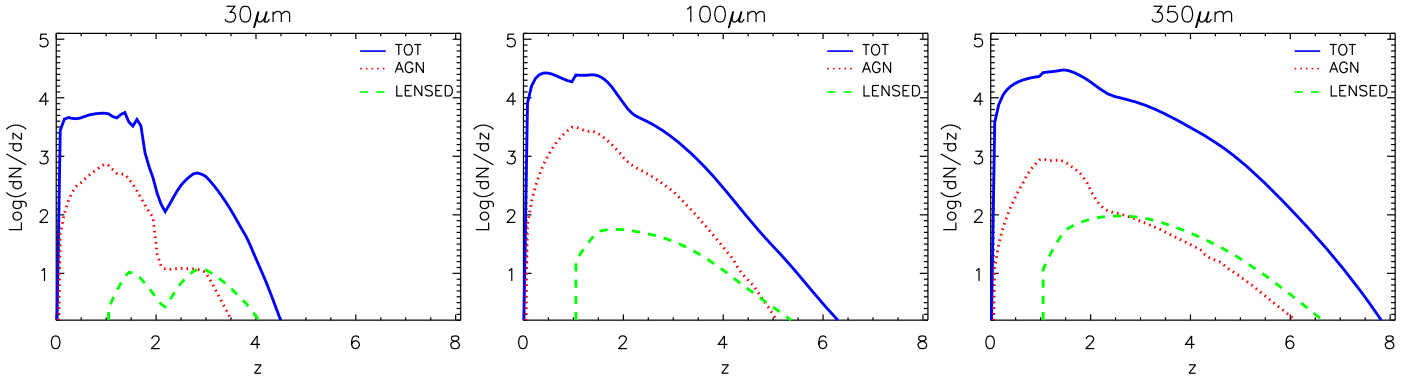

Figure 10. Predicted redshift distributions at 30, 100, and 350 μm (from left to right) at the detection limits of the reference survey (0.14, 0.21, 0.33) mJy, respectively. The deep hollow at $z \sim 2$ in the 30 μm distribution is due to the strong silicate absorption around 9.7 μm. The inflection point at $z \simeq 2$–2.5, seen at 100 and 350 μm, corresponds to the transition from starburst to proto-spheroid dominance.

to IR lines excited by AGNs, working out relations between the line and AGN bolometric luminosity. In another paper, we derived relationships between the main IR lines and the SFR, complementing the available data with extensive simulations that took into account the effect of dust extinction (M. Bonato et al. 2014b). Finally, we updated some of these relations, taking into account more recent data, and determined relations for additional lines (M. Bonato et al. 2019).

3.2. Results

Figure 9 shows the integral counts predicted by the model (described in the previous subsection) at 30, 100, and 350 μm, including the contributions of AGNs and of strongly lensed galaxies. The vertical black lines correspond to the 5σ detection limits of our reference survey.

At these limits, the counts have already substantially flattened, so going wider is far more advantageous than going deeper. The FIR wavelength range encompasses the peak of the cosmic IR background, occurring at $\sim$200 μm (D. J. Fixsen et al. 1998). We expect that the reference survey will yield approximately 8500, 46,000, and 61,000 $\geqslant$5σ detections at 30, 100, and 350 μm, respectively. These sources contribute $\sim$0.02, 0.35, and 0.75 MJy sr^{-1} at 30, 100, and 350 μm, respectively, i.e., $\sim$60%, 87%, and 84% of the cosmic IR background intensity predicted by the model, which is consistent with the fit to the observational intensity estimate given by Equation (5) of D. J. Fixsen et al. (1998).

The number of strongly lensed galaxies is small at 30 μm ($\simeq$20 sources, 0.23%) and increases to $\simeq$120 (0.26%) at 100 μm and to $\simeq$260 (0.42%) at 350 μm. At the latter wavelength, 120 strongly lensed galaxies are detected at $\geqslant$20σ, implying that multiple images will be visible (see the discussion in the Appendix of C. Mancuso et al. 2015). Taking advantage of the gravitational stretching of the images, it will be possible to investigate their internal structure.

At 30 μm, the global AGN fraction of detected sources is $\simeq$9%, increasing to $\simeq$25% above 3 mJy. Although the fraction steadily decreases with increasing wavelength due to the warmer AGN MIR/FIR SED compared to that of dusty galaxies, the total AGN number peaks at around 100 μm, with $\simeq$4100 detections ($\simeq$740 detections at 30 μm and $\simeq$1200 at 350 μm). We note that these AGN counts are computed in terms of the flux density from the active nucleus only. The number of sources hosting an AGN detectable in other wave bands (X-ray, optical, near-IR/MIR) is substantially larger but difficult to quantify.

Figure 10 shows the predicted redshift distributions at 30, 100, and 350 μm of sources above the 5σ detection limits of the reference survey. The distributions extend to higher and higher redshifts with increasing wavelength, reaching the EoR at 350 μm. There are $\simeq$160, 1100, and 7600 galaxies at $z \geqslant 3$, respectively, at the three wavelengths.

Figure 11 shows the minimum IR luminosity of SFGs and the minimum bolometric luminosity of AGNs, detectable at 5σ by the reference survey. The large improvement over Herschel surveys (the dotted–dashed green lines) allows a big step

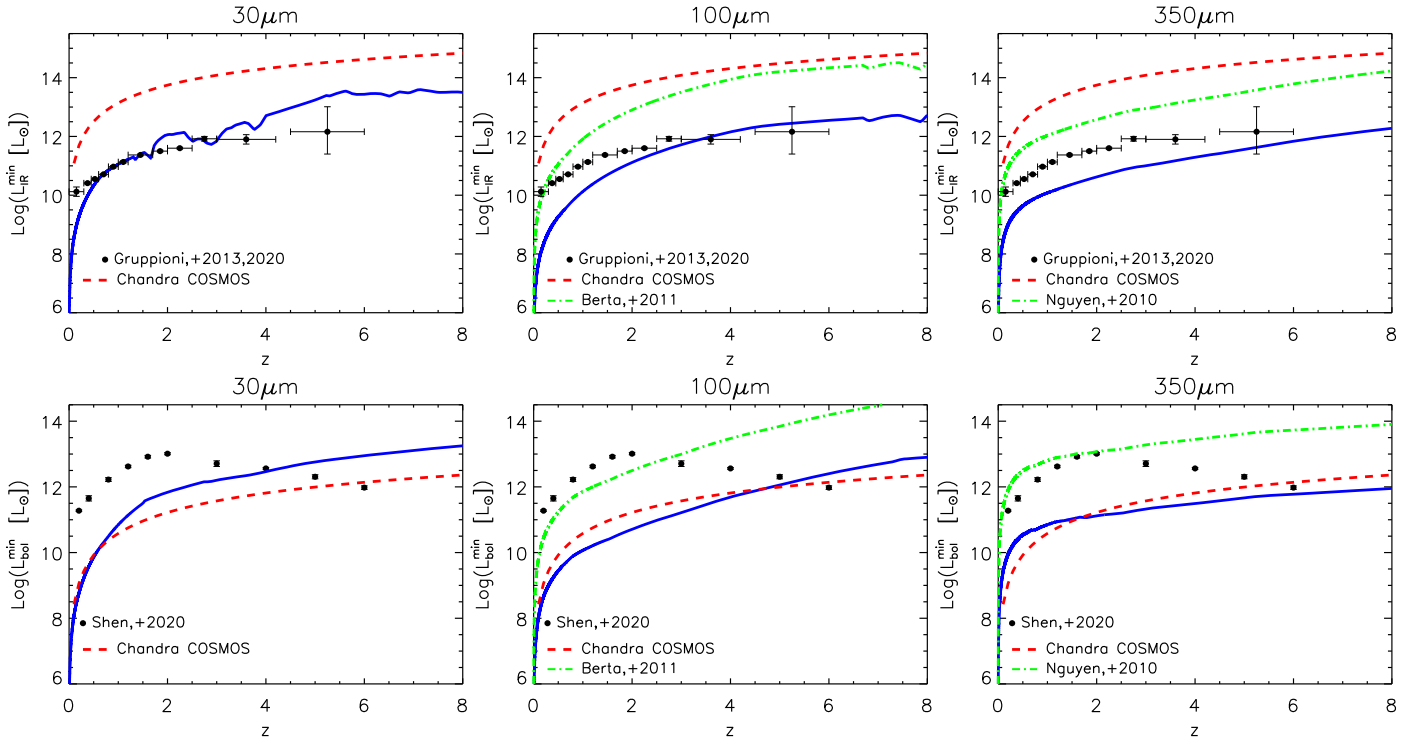

Figure 11. Upper panels: predicted minimum IR (8–1000 μm) luminosity of SFGs detected by the reference survey at 30, 100, and 350 μm (blue curves) as a function of redshift. The dotted–dashed green line shows, for comparison, the minimum luminosity corresponding to the 80% completeness of the PEP survey of the COSMOS field (9 mJy; S. Berta et al. 2011) at 100 μm and that corresponding to the Herschel SPIRE 5σ confusion limit at 350 μm (31.5 mJy; H. T. Nguyen et al. 2010). The points with error bars show the characteristic luminosity, $L_\star(z)$, of the Schechter fit of the IR LF by C. Gruppioni et al. (2013); the point at $4.5 \leqslant z \leqslant 6$ is from C. Gruppioni et al. (2020). The dashed red line shows an estimate of the IR luminosity of the SFG hosting an AGN having a 2–10 keV X-ray luminosity at the 90% completeness detection limit of the Chandra COSMOS legacy survey (7.8×10^{-15} erg cm^{-2} s^{-1}; Table 2 of S. Puccetti et al. 2009), as a function of z. To compute the K-correction, we assumed a power-law energy spectrum with a spectral index of -0.4, the slope of the cosmic X-ray background in this energy range; this represents an effective spectral index, taking into account both obscured and unobscured AGNs. Lower panels: minimum bolometric luminosity of AGNs detectable by the reference survey at the three wavelengths as a function of redshift (solid blue line). The dashed red line shows, for comparison, an estimate of the minimum bolometric luminosity of AGNs detected in X-rays by the Chandra COSMOS legacy survey, as a function of z; it was obtained by applying the bolometric correction of 22.4 (from C.-T. J. Chen et al. 2013) to the 2–10 keV luminosity, computed as described above. The data points show the characteristic AGN bolometric luminosity up to $z = 6$ derived by X. Shen et al. (2020). Similar to the upper panels, the dotted–dashed green line shows, for comparison, the minimum bolometric luminosity corresponding to the 80% completeness of the PEP survey of the COSMOS field (9 mJy; S. Berta et al. 2011) at 100 μm and that corresponding to the Herschel SPIRE 5σ confusion limit at 350 μm (31.5 mJy; H. T. Nguyen et al. 2010).

forward in the observational investigation of the co-evolution of the SFR and of the accretion rate onto the SMBH, as discussed in the next section. The minimum detectable IR luminosity of galaxies is much lower than that corresponding to the minimum X-ray luminosity detected by the deep Chandra COSMOS Legacy Survey (F. Civano et al. 2016), according to the SFR/accretion rate correlation by C.-T. J. Chen et al. (2013). At the longest wavelengths, exemplified by the 350 μm panel, the survey reaches luminosities substantially fainter than the characteristic IR luminosity, $L_\star(z)$, of SFGs over the redshift range at which it has been estimated. This will allow us to put on much more solid ground the determination of the redshift-dependent IR LF and the corresponding obscured cosmic SFR density. This will crucially complement previous studies at the high-z end, which so far have been mostly based on UV-selected samples of massive galaxies (see, e.g., ALPINE at $z = 4$–6—C. Gruppioni et al. 2020; Y. Khusanova et al. 2021; and REBELS at $z \sim 7$—H. S. B. Algera et al. 2023; L. Barrufet et al. 2023; see also J. A. Zavala et al. 2021).

The lower panels of Figure 11 show that the reference survey has a depth comparable to that of the Chandra COSMOS Legacy Survey (F. Civano et al. 2016) in terms of the AGN bolometric luminosity, making it possible to get a comprehensive view of the AGN SED. Except at the highest redshifts, both surveys reach luminosities well below the characteristic bolometric luminosity $L_{\rm bol\ AGN,\star}(z)$ derived by X. Shen et al. (2020) up to $z = 6$.

The left-hand panels of Figure 12 show the predicted integral counts of SFGs and AGNs (upper and lower panels, respectively) detected in their brightest lines. The right-hand panels show the corresponding redshift distributions at the detection limit of the reference survey. We note that the PAH band at 12.7 μm[14] is detectable only at $z \gtrsim 1$. We expect a significant number of detections in this line up to $z > 6$; in the [O III] 51.81 μm line up to $z \gtrsim 5$; and in the [Si II] 34.82 μm and the [O I] 61.18 μm lines up to $z \gtrsim 4$.

The AGN lines are relatively weak. The slope of the counts below the detection limit of the reference survey is steeper than that of SFGs, implying that in this case there is a gain in going deeper. We expect fewer than 100 detections in the [O IV] 25.89 μm line at $z \lesssim 2$ with the reference survey. As mentioned in Section 1, dust-enshrouded AGNs at higher redshift may be uncovered through the intensity ratios of PAH features. Also, information on AGNs can be retrieved by

[14] We expect comparable numbers of detections in the other PAH lines listed in Table 1 and we choose PAH 12.7 μm as being representative of all of them.

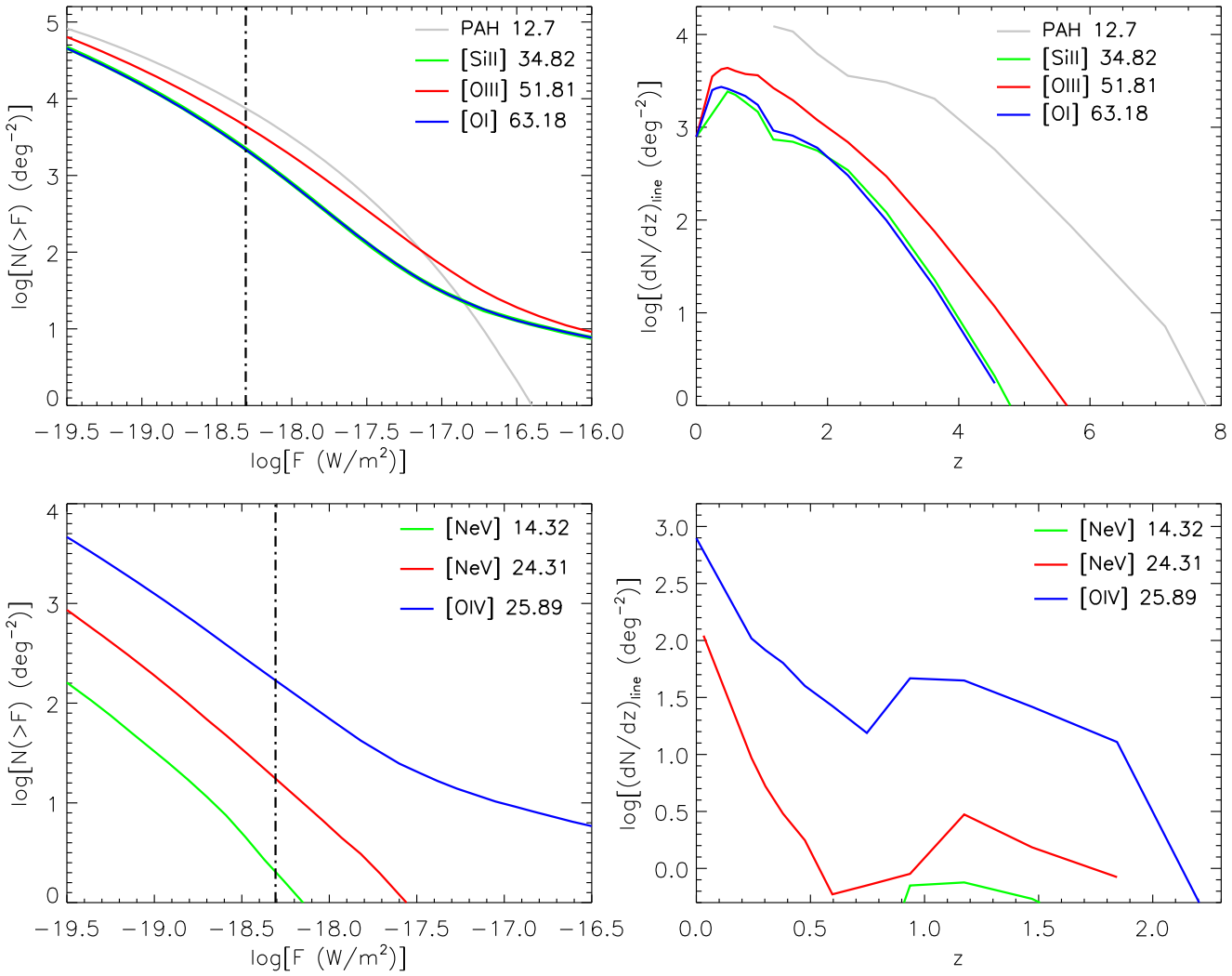

Figure 12. Predicted integral number counts (left) and redshift distributions (right) for sources detected in line emission by the reference survey. In the top left panel, the integral counts of the [Si II] line are superimposed on those of the [O I] line. The dotted–dashed vertical black lines in the left-hand panels show the 5σ detection limit (the mean detection limit for the reference survey and for the fine-structure lines among the four spectral bands). Upper panels: SFGs detected in one or more bright lines, with spectral resolution $R = 500$ for fine-structure lines and $R = 50$ for the PAH band. The inflection points of the redshift distributions are due to the transition from the first band (25–50 μm) to the more sensitive second band (50–100 μm). Lower panels: same as in the upper panels, but for AGN lines. The transition from the first to the second band is responsible for the bump at $z \gtrsim 1$.

stacking fluxes at the positions of sources detected in the continuum.

4. Discussion

A sensitive FIR space mission achieving subarcsecond resolution is an essential complement to JWST and ALMA if we are to definitively address the Astro2020 Decadal Survey (National Academies of Sciences, Engineering, & Medicine 2021) imperative to understand the co-evolution of galaxies and their central SMBHs. Such a mission would allow us to study the dusty ISM of SFGs and heavily obscured AGNs at crucial wavelengths for individual sources (both galaxies and AGNs) out to high redshifts. Continuum FIR observations are essential for determining the total IR luminosity of SFGs.

As illustrated by Figure 13, the much better angular resolution of the proposed SPIRIT interferometer effectively eliminates extragalactic source confusion. Figure 13 shows the dependence on the effective telescope diameter or maximum interferometer baseline, D, of $S_{\rm conf} = 5\,\sigma_{\rm conf}$, $\sigma_{\rm conf}$ being the rms confusion noise given by

$$\sigma^2_{\rm conf} = \omega_{\rm eff} \int_0^{S_{\rm conf}} \frac{dN}{dS}\, S^2\, dS, \tag{1}$$

where, assuming a Gaussian beam, the effective solid angle is

$$\omega_{\rm eff} = \frac{\pi}{2\ln 2}\left(\frac{\rm FWHM}{2}\right)^2, \tag{2}$$

with FWHM $= 1.2\,\lambda/D$. The three curves in Figure 13 show, from bottom to top, $S_{\rm conf}(D)$ for $\lambda = 30$, 100, and 350 μm, respectively.

An FIR interferometer will allow us to extend the determination of the IR LFs of SFGs and of AGNs down to much fainter luminosities, whereas smaller, confusion-limited telescopes see only relatively bright cosmological sources and may underestimate or overestimate line strengths. We have shown that, for the considered observing time, the number of detections is maximized by a survey of 0.5 deg^2, approximately the same area as the COSMOS-Web JWST treasury program (C. M. Casey et al. 2023), covering wavelengths from 25 to

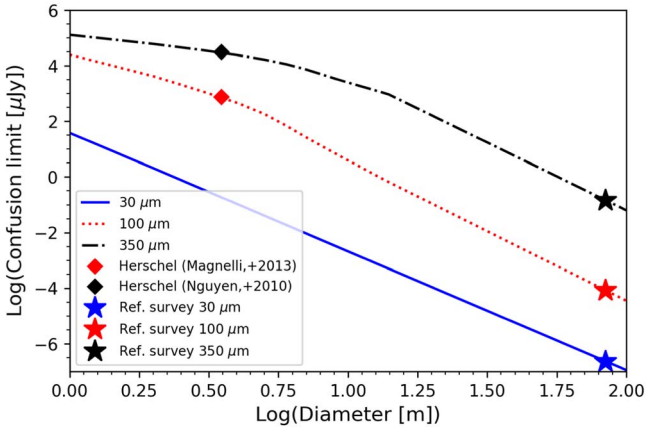

Figure 13. Confusion limit, $S_{\rm conf}$ (5σ), at 30, 100, and 350 μm as a function of the effective telescope diameter or maximum interferometer baseline, D. The diamonds show the measured confusion limits of Herschel SPIRE at 350 μm (31.5 mJy; black diamond; H. T. Nguyen et al. 2010) and of Herschel PACS at 100 μm (0.75 mJy; red diamond; B. Magnelli et al. 2013). The improved resolution of the interferometer results in a dramatic fall of confusion limits. The stars represent the confusion limits for the proposed survey. The model, used to compute $S_{\rm conf}$ as a function of D at the three wavelengths, shown by the solid blue line, by the dotted red line, and by the dotted–dashed black line, yields $S_{\rm conf} = 2.3 \times 10^{-7}$, 8.3×10^{-5}, and 0.14 μJy at 30, 100, and 350 μm, respectively. Confusion is negligible at these levels.

400 μm. We have calculated the expected source detections for a survey of 1000 hr (allowing for 90% observing efficiency) over such an area, down to the 5σ detection limits of (0.10, 0.14, 0.21, 0.33) mJy in the continuum in the 25–50, 50–100, 100–200, and 200–400 μm wavelength intervals, respectively.

At 350 μm, this reference survey will detect ∼61,000 SFGs out to redshift $z \simeq 6$, and perhaps to $z = 7$–8; about 7600 galaxies will be at $z > 3$. A few hundred galaxies should be strongly lensed; about half of these will be detected at $\gtrsim 20\sigma$, so that it will be possible to take advantage of the gravitational stretching of the images to further improve the resolution at which the internal structure can be studied.

A comparison, shown in Figure 11, with the characteristic IR luminosity of SFGs as a function of redshift, $L_{\rm IR,\star}(z)$, estimated by C. Gruppioni et al. (2013) and C. Gruppioni et al. (2020), shows that, at least at the longest wavelengths, the proposed survey will reach luminosities fainter than $L_{\rm IR,\star}(z)$, thus allowing us to investigate typical SFGs at high z. This survey will also resolve the sources contributing up to ∼87% of the cosmic IR background at its peak.

In the obscured AGN case, the FIR interferometer will go much deeper than ALMA and provide unique information on the global energetics of dust-obscured nuclear activity, hence on the AGN accretion history. The number of AGN detections is highest around 100 μm, where the reference survey is predicted to detect ∼4100 such objects at redshifts of up to $z \sim 4$–4.5. At longer wavelengths, we expect AGN detections up to $z \sim 5.5$–6.

Again at the longest FIR wavelengths, the AGN bolometric LF can be determined down to below the characteristic bolometric luminosity $L_{\rm bol\ AGN,\star}(z)$ derived by X. Shen et al. (2020) up to $z = 6$ (lower panels of Figure 11). This amounts to getting a direct, solid, quantitative assessment of the cosmic star formation and obscured accretion history; presently, both of them are poorly constrained for $z > 2$.

Another possible breakthrough is the understanding of complex facets of galaxy–AGN co-evolution. The tight correlations between the mass of the SMBH and the global properties of the spheroidal component of the host galaxy (L. Ferrarese & H. Ford 2005; J. Kormendy & L. C. Ho 2013), and the broad parallelism of the cosmic history of BH and stellar mass growth (F. Shankar et al. 2009), imply a strong evolutionary connection. However, the physical processes responsible for it are still being debated. These include various kinds of feedback mechanisms (J. Silk & M. J. Rees 1998; A. C. Fabian 1999, 2012; A. King 2003; G. L. Granato et al. 2004; N. Murray et al. 2005; D. Farrah et al. 2012; R. C. McQuillin & D. E. McLaughlin 2012), capable of controlling the star formation and the SMBH accretion rate. Alternatively, the evolution of both components can be regulated by galaxy properties that determine how the gas feeds star formation and accretion (D. Anglés-Alcázar et al. 2015; Q. Ni et al. 2021). Another possible explanation links the correlations to the effect of mergers (K. Jahnke & A. V. Macciò 2011; A. W. Graham & N. Sahu 2023).

Also, models predict different star formation and accretion histories as a function of galactic age, with feedback either inducing or quenching star formation, but observational verifications have remained elusive. A direct test of galaxy/AGN co-evolution models (G. L. Granato et al. 2004; T. Di Matteo et al. 2005; A. Lapi et al. 2006, 2014; M. Hirschmann et al. 2014; R. Weinberger et al. 2017) can be performed by studying the correlation between star formation and accretion rates (C.-T. J. Chen et al. 2013; I. Delvecchio et al. 2015; G. Rodighiero et al. 2015; G. Lanzuisi et al. 2017; J. Aird et al. 2019; H. Suh et al. 2019; R. Carraro et al. 2020; I. E. López et al. 2023; G. Mountrichas & F. Shankar 2023). To this end, we can exploit the X-ray luminosity, a clean tracer of nuclear emission, i.e., of the BHAR, and the FIR luminosity, an efficient indicator of the host galaxy SFR. Most of the cited studies have targeted the COSMOS field, taking advantage of the extensive multifrequency photometry and spectroscopic information available with a unique combination of depth and area ($\simeq 2$ deg^2).

The Chandra COSMOS Legacy Survey (F. Civano et al. 2016) has provided a deep, uniform, X-ray coverage of the field. The field was also covered by the Herschel Photodetector Array Camera and Spectrometer (PACS) Evolutionary Probe (PEP) survey (S. Berta et al. 2011; D. Lutz et al. 2011) and by the Herschel Multi-tiered Extragalactic Survey (HerMES; S. J. Oliver et al. 2012). However, a minor fraction of sources have both Herschel and X-ray measurements. For example, only 27% of the X-ray-selected sample by H. Suh et al. (2019) have a detection at least at one Herschel wavelength, implying that estimates of the SFR are quite uncertain. Conversely, we have found that only 12% of galaxies detected at 250 μm by the HerMES survey of the COSMOS field have a Chandra detection within 10″. Thus, the study of star formation in galaxies hosting AGNs or of the AGN activity in SFGs has been so far hampered by selection biases (the different selections favor either the brighter X-ray sources or the higher SFRs that may not be representative of the general population). Various techniques (e.g., stacking and SED fitting based on templates) have been applied to make up for missing data. Conflicting results have been obtained. Some studies have reported evidence of a correlation between BHAR and SFR (C.-T. J. Chen et al. 2013;

J. Aird et al. 2019; R. Carraro et al. 2020; O. Torbaniuk et al. 2021; G. Mountrichas & F. Shankar 2023); others have concluded that SFRs are independent of AGN activity (M. Azadi et al. 2015; F. Stanley et al. 2015; H. Suh et al. 2019; M. Symeonidis et al. 2022); still others have found a lack of star formation in the host galaxies of X-ray quasars (A. J. Barger et al. 2015).

While the correlation between SFR and BHAR provides valuable insights, it is crucial to consider additional factors—such as stellar masses, ages, and metallicities—to draw more definitive conclusions about the underlying physical processes. Interferometric surveys can provide robust stellar masses and FIR line-based ages and metallicities, simultaneously with SFRs and BHARs.

As illustrated by Figure 11, the reference survey will reach, at all FIR wavelengths and at all redshifts, IR luminosities well below those of SFGs hosting AGNs with a 2–10 keV X-ray luminosity at the 90% completeness detection limit of the Chandra COSMOS legacy survey, according to the correlation between AGN bolometric luminosity and SFR reported by C.-T. J. Chen et al. (2013). Although such correlation has a large dispersion and even its reality is controversial, the reference survey would allow decisive progress on our understanding of galaxy–BH co-evolution. In particular, we will be able to derive information on the growth timescales of stellar and BH masses and on the relative importance of positive and negative feedback.

The spectroscopy we envisage will measure the physical conditions of dust-obscured atomic and ionized gas phases. The MIR/FIR fine-structure lines provide unique information on the dust-obscured phases of the ISM, which by definition are invisible in the optical. The reference survey will detect thousands of galaxies in the [O I] 63.18 μm, [Si II] 34.82 μm, and [O III] 51.81 μm lines. The [O I] line is an important coolant of neutral gas; we predict about 1000 detections in this line up to $z \simeq 1$, a few hundred at $1 < z < 3$, and some detections up to $z \simeq 4$. The [Si] line comes from moderately ionized gas; the redshift distribution of galaxies detected in this line is similar to that of the [O I] line. The [O III] line traces dust in the ionized phase; it is detectable by the reference survey up to $z \simeq 5$, but its redshift distribution peaks at $z \lesssim 1$, where we expect thousands of detections. The strong PAH bands are visible up to $\simeq$6 and are good SFR measures. The lines with high excitation potential, such as [O IV] 25.89 μm and [Ne V] at 14.32 and 24.31 μm, are indicative of AGN activity. The reference survey will detect the [O IV] line for almost 100 AGNs at $z \lesssim 2$. The line intensity is well correlated with the BHAR. Simultaneous measurements of this line and of SFR tracers will provide insights into galaxy–AGN co-evolution.

The spectral resolution of an interferometer like SPIRIT will allow us to exploit the brightest FIR lines to measure gas velocities, shedding light on inflows and outflows and on the interplay of different gas phases. Powerful outflows, driven by supernova explosions or by AGN activity, have a key role in controlling galaxy evolution via positive or negative feedback.

5. Conclusions

In summary, an FIR space mission with high angular resolution is crucial for advancing our understanding of the co-evolution of galaxies and SMBHs. The key findings from our analysis are summarized in the following points:

1. An astronomical background-limited small telescope preferentially detects bright (luminous and low-z) galaxies.
2. An FIR high-resolution interferometer significantly reduces extragalactic source confusion and is crucial to addressing the co-evolution of galaxies and SMBHs, providing key insights that complement JWST and ALMA findings.
3. The proposed FIR survey will detect tens of thousands of SFGs and thousands of AGNs up to $z \sim 6$, in multiple FIR lines (e.g., [C II], [O I], and [C I]) and continuum.
4. The survey will reach luminosities below the characteristic IR luminosity at high z, extending IR LF determinations to much fainter levels and resolving up to 87% of the cosmic IR background.
5. The synergy of high spectral resolution, line sensitivity, and extensive spectral coverage will enable detailed insights into the physical properties, such as the temperature, density, and metallicity of the ISM up to high redshift.

Acknowledgments

We are grateful to the anonymous referee for a careful reading of the manuscript and many useful comments. M.B. acknowledges support from INAF under the mini-grant "A systematic search for ultra-bright high-z strongly lensed galaxies in Planck catalogues". We thank Dr. Alexander Kashlinsky for developing the original sky simulation code cited in Section 2 and Ms. Aláine Lee for assisting with code modifications during a summer internship at NASA's Goddard Space Flight Center.

ORCID iDs

Matteo Bonato https://orcid.org/0000-0001-9139-2342
Gianfranco De Zotti https://orcid.org/0000-0003-2868-2595
Irene Shivaei https://orcid.org/0000-0003-4702-7561
C. Megan Urry https://orcid.org/0000-0002-0745-9792
Duncan Farrah https://orcid.org/0000-0003-1748-2010
Susanne Aalto https://orcid.org/0000-0002-5828-7660
David B. Sanders https://orcid.org/0000-0002-1233-9998

References

Adams, N. J., Conselice, C. J., Ferreira, L., et al. 2023, MNRAS, 518, 4755
Aird, J., Coil, A. L., & Georgakakis, A. 2019, MNRAS, 484, 4360
Algera, H. S. B., Inami, H., Oesch, P. A., et al. 2023, MNRAS, 518, 6142
Algera, H. S. B., Inami, H., Sommovigo, L., et al. 2024, MNRAS, 527, 6867
Álvarez-Márquez, J., Burgarella, D., Heinis, S., et al. 2016, A&A, 587, A122
Ananna, T. T., Treister, E., Urry, C. M., et al. 2019, ApJ, 871, 240
Anglés-Alcázar, D., Özel, F., Davé, R., et al. 2015, ApJ, 800, 127
Auge, C., Sanders, D., Urry, C., Cappelluti, N. & Accretion History of AGN (AHA) Team 2022, AAS Meeting, 240, 335.07
Azadi, M., Aird, J., Coil, A. L., et al. 2015, ApJ, 806, 187
Bakx, T. J. L. C., Tamura, Y., Hashimoto, T., et al. 2020, MNRAS, 493, 4294
Barger, A. J., Cowie, L. L., Owen, F. N., et al. 2015, ApJ, 801, 87
Barro, G., Kriek, M., Pérez-González, P. G., et al. 2016, ApJL, 827, L32
Barro, G., Pérez-González, P. G., Cava, A., et al. 2019, ApJS, 243, 22
Barrufet, L., Oesch, P. A., Bouwens, R., et al. 2023, MNRAS, 522, 3926
Berta, S., Magnelli, B., Nordon, R., et al. 2011, A&A, 532, A49
Béthermin, M., Fudamoto, Y., Ginolfi, M., et al. 2020, A&A, 643, A2
Bianchi, S., Maiolino, R., & Risaliti, G. 2012, AdAst, 2012, 782030
Bonato, M., De Zotti, G., Leisawitz, D., et al. 2019, PASA, 36, e017
Bonato, M., Negrello, M., Cai, Z. Y., et al. 2014a, MNRAS, 444, 3446
Bonato, M., Negrello, M., Cai, Z. Y., et al. 2014b, MNRAS, 438, 2547
Bonato, M., Prandoni, I., De Zotti, G., et al. 2021, A&A, 656, A48

Bouwens, R., González-López, J., Aravena, M., et al. 2020, ApJ, 902, 112
Bouwens, R., Illingworth, G., Oesch, P., et al. 2023, MNRAS, 523, 1009
Bouwens, R. J., Smit, R., Schouws, S., et al. 2022, ApJ, 931, 160
Bouwens, R. J., Stefanon, M., Brammer, G., et al. 2023, MNRAS, 523, 1036
Brandt, W. N., Hornschemeier, A. E., Alexander, D. M., et al. 2001, AJ, 122, 1
Cai, Z.-Y., Lapi, A., Xia, J.-Q., et al. 2013, ApJ, 768, 21
Cappelluti, N., Brusa, M., Hasinger, G., et al. 2009, A&A, 497, 635
Cappelluti, N., Hasinger, G., Brusa, M., et al. 2007, ApJS, 172, 341
Carilli, C. L., & Walter, F. 2013, ARA&A, 51, 105
Carnall, A. C., McLeod, D. J., McLure, R. J., et al. 2023, MNRAS, 520, 3974
Carniani, S., Ferrara, A., Maiolino, R., et al. 2020, MNRAS, 499, 5136
Carraro, R., Rodighiero, G., Cassata, P., et al. 2020, A&A, 642, A65
Casey, C. M., Kartaltepe, J. S., Drakos, N. E., et al. 2023, ApJ, 954, 31
Casey, C. M., Zavala, J. A., Manning, S. M., et al. 2021, ApJ, 923, 215
Chen, C.-C., Liao, C.-L., Smail, I., et al. 2022, ApJ, 929, 159
Chen, C.-T. J., Hickox, R. C., Alberts, S., et al. 2013, ApJ, 773, 3
Ciotti, L., & Bertin, G. 1999, A&A, 352, 447
Civano, F., Elvis, M., Brusa, M., et al. 2012, ApJS, 201, 30
Civano, F., Marchesi, S., Comastri, A., et al. 2016, ApJ, 819, 62
Clemens, M. S., Negrello, M., De Zotti, G., et al. 2013, MNRAS, 433, 695
Clements, D. L., Rigby, E., Maddox, S., et al. 2010, A&A, 518, L8
Coppin, K., Chapin, E. L., Mortier, A. M. J., et al. 2006, MNRAS, 372, 1621
Davis, M., Guhathakurta, P., Konidaris, N. P., et al. 2007, ApJL, 660, L1
Dekel, A., Sarkar, K. C., Birnboim, Y., Mandelker, N., & Li, Z. 2023, MNRAS, 523, 3201
Delvecchio, I., Lutz, D., Berta, S., et al. 2015, MNRAS, 449, 373
Di Matteo, T., Springel, V., & Hernquist, L. 2005, Natur, 433, 604
Dole, H., Rieke, G. H., Lagache, G., et al. 2004, ApJS, 154, 93
Donnan, C. T., McLeod, D. J., Dunlop, J. S., et al. 2023a, MNRAS, 518, 6011
Donnan, C. T., McLeod, D. J., McLure, R. J., et al. 2023b, MNRAS, 520, 4554
Donnan, C. T., McLure, R. J., Dunlop, J. S., et al. 2024, MNRAS, 533, 3222
Donnellan, J. M. S., Oliver, S. J., Béthermin, M., et al. 2024, MNRAS, 532, 1966
Eales, S., Dunne, L., Clements, D., et al. 2010, PASP, 122, 499
Eisenstein, D. J., Willott, C., Alberts, S., et al. 2023, arXiv:2306.02465
Elvis, M., Civano, F., Vignali, C., et al. 2009, ApJS, 184, 158
Fabian, A. C. 1999, MNRAS, 308, L39
Fabian, A. C. 2012, ARA&A, 50, 455
Faisst, A. L., Schaerer, D., Lemaux, B. C., et al. 2020, ApJS, 247, 61
Farrah, D., Bernard-Salas, J., Spoon, H. W. W., et al. 2007, ApJ, 667, 149
Farrah, D., Lebouteiller, V., Spoon, H. W. W., et al. 2013, ApJ, 776, 38
Farrah, D., Urrutia, T., Lacy, M., et al. 2012, ApJ, 745, 178
Ferrara, A., Pallottini, A., & Dayal, P. 2023, MNRAS, 522, 3986
Ferrarese, L., & Ford, H. 2005, SSRv, 116, 523
Finkelstein, S. L., Bagley, M. B., Ferguson, H. C., et al. 2023, ApJL, 946, L13
Fixsen, D. J., Dwek, E., Mather, J. C., Bennett, C. L., & Shafer, R. A. 1998, ApJ, 508, 123
Galametz, A., Grazian, A., Fontana, A., et al. 2013, ApJS, 206, 10
García-Bernete, I., Rigopoulou, D., Aalto, S., et al. 2022, A&A, 663, A46
Giavalisco, M., Ferguson, H. C., Koekemoer, A. M., et al. 2004, ApJL, 600, L93
González-Solares, E. A., Irwin, M., McMahon, R. G., et al. 2011, MNRAS, 416, 927
Graham, A. W., & Sahu, N. 2023, MNRAS, 518, 2177
Granato, G. L., De Zotti, G., Silva, L., Bressan, A., & Danese, L. 2004, ApJ, 600, 580
Greenslade, J., Clements, D. L., Petitpas, G., et al. 2020, MNRAS, 496, 2315
Grogin, N. A., Kocevski, D. D., Faber, S. M., et al. 2011, ApJS, 197, 35
Gruppioni, C., Béthermin, M., Loiacono, F., et al. 2020, A&A, 643, A8
Gruppioni, C., Pozzi, F., Rodighiero, G., et al. 2013, MNRAS, 432, 23
Gullberg, B., Smail, I., Swinbank, A. M., et al. 2019, MNRAS, 490, 4956
Guo, Y., Ferguson, H. C., Giavalisco, M., et al. 2013, ApJS, 207, 24
Harikane, Y., Ouchi, M., Oguri, M., et al. 2023, ApJS, 265, 5
Hasinger, G. 2008, A&A, 490, 905
Hasinger, G., Altieri, B., Arnaud, M., et al. 2001, A&A, 365, L45
Hasinger, G., Cappelluti, N., Brunner, H., et al. 2007, ApJS, 172, 29
Heywood, I., Jarvis, M. J., Hale, C. L., et al. 2022, MNRAS, 509, 2150
Hickox, R. C., & Alexander, D. M. 2018, ARA&A, 56, 625
Hirschmann, M., De Lucia, G., Wilman, D., et al. 2014, MNRAS, 444, 2938
Hodge, J. A., & da Cunha, E. 2020, RSOS, 7, 200556
Hodge, J. A., Smail, I., Walter, F., et al. 2019, ApJ, 876, 130
Hurley, P. D., Oliver, S., Betancourt, M., et al. 2017, MNRAS, 464, 885
Jahnke, K., & Macciò, A. V. 2011, ApJ, 734, 92
Kelsall, T., Weiland, J. L., Franz, B. A., et al. 1998, ApJ, 508, 44
Khusanova, Y., Bethermin, M., Le Fèvre, O., et al. 2021, A&A, 649, A152
King, A. 2003, ApJL, 596, L27
Kocevski, D. D., Barro, G., McGrath, E. J., et al. 2023, ApJL, 946, L14
Koekemoer, A. M., Faber, S. M., Ferguson, H. C., et al. 2011, ApJS, 197, 36
Kondapally, R., Best, P. N., Hardcastle, M. J., et al. 2021, A&A, 648, A3
Konidaris, N. P., Guhathakurta, P., Bundy, K., et al. 2007, ApJL, 660, L7
Kormendy, J., & Ho, L. C. 2013, ARA&A, 51, 511
Lagache, G., Puget, J.-L., & Dole, H. 2005, ARA&A, 43, 727
Laird, E. S., Nandra, K., Georgakakis, A., et al. 2009, ApJS, 180, 102
Laloux, B., Georgakakis, A., Andonie, C., et al. 2023, MNRAS, 518, 2546
Lang, P., Schinnerer, E., Smail, I., et al. 2019, ApJ, 879, 54
Lanzuisi, G., Delvecchio, I., Berta, S., et al. 2017, A&A, 602, A123
Lapi, A., Raimundo, S., Aversa, R., et al. 2014, ApJ, 782, 69
Lapi, A., Shankar, F., Mao, J., et al. 2006, ApJ, 650, 42
Le Fèvre, O., Béthermin, M., Faisst, A., et al. 2020, A&A, 643, A1
Lehmer, B. D., Xue, Y. Q., Brandt, W. N., et al. 2012, ApJ, 752, 46
Leisawitz, D., Baker, C., Barger, A., et al. 2007, AdSpR, 40, 689
Leisawitz, D., Hyde, T. T., Rinehart, S. A., & Weiss, M. 2008, Proc. SPIE, 7010, 701028
Leisawitz, D. & PIRIT Origins Probe Mission Concept Study Team 2009, The Space Infrared Interferometric Telescope (SPIRIT): A Far-IR Observatory for High-resolution Imaging and Spectroscopy, Goddard Space Flight Center
Lemaux, B. C., Le Floc'h, E., Le Fèvre, O., et al. 2014, A&A, 572, A90
Leung, G. C. K., Bagley, M. B., Finkelstein, S. L., et al. 2023, ApJL, 954, L46
Li, A. 2020, NatAs, 4, 339
Liu, T., Tozzi, P., Wang, J.-X., et al. 2017, ApJS, 232, 8
Loiacono, F., Decarli, R., Gruppioni, C., et al. 2021, A&A, 646, A76
López, I. E., Brusa, M., Bonoli, S., et al. 2023, A&A, 672, A137
Lovell, M. R., Hellwing, W., Ludlow, A., et al. 2020, MNRAS, 498, 702
Luo, B., Brandt, W. N., Xue, Y. Q., et al. 2017, ApJS, 228, 2
Lutz, D. 2014, ARA&A, 52, 373
Lutz, D., Poglitsch, A., Altieri, B., et al. 2011, A&A, 532, A90
Lyu, J., & Rieke, G. 2022, Univ, 8, 304
Madau, P., & Dickinson, M. 2014, ARA&A, 52, 415
Magnelli, B., Popesso, P., Berta, S., et al. 2013, A&A, 553, A132
Mancuso, C., Lapi, A., Cai, Z.-Y., et al. 2015, ApJ, 810, 72
Marrone, D. P., Spilker, J. S., Hayward, C. C., et al. 2018, Natur, 553, 51
Mauduit, J. C., Lacy, M., Farrah, D., et al. 2012, PASP, 124, 714
Mauerhofer, V., & Dayal, P. 2023, MNRAS, 526, 2196
McKinney, J., Manning, S. M., Cooper, O. R., et al. 2023, ApJ, 956, 72
McLeod, D. J., Donnan, C. T., McLure, R. J., et al. 2024, MNRAS, 527, 5004
McQuillin, R. C., & McLaughlin, D. E. 2012, MNRAS, 423, 2162
Meléndez, M., Kraemer, S. B., Armentrout, B. K., et al. 2008, ApJ, 682, 94
Mountrichas, G., & Shankar, F. 2023, MNRAS, 518, 2088
Murray, N., Quataert, E., & Thompson, T. A. 2005, ApJ, 618, 569
Nandra, K., Laird, E. S., Aird, J. A., et al. 2015, ApJS, 220, 10
National Academies of Sciences, Engineering, and Medicine 2021, Pathways to Discovery in Astronomy and Astrophysics for the 2020s (Washington, DC: The National Academies Press)
Nayyeri, H., Hemmati, S., Mobasher, B., et al. 2017, ApJS, 228, 7
Negrello, M., Amber, S., Amvrosiadis, A., et al. 2017, MNRAS, 465, 3558
Negrello, M., Hopwood, R., De Zotti, G., et al. 2010, Sci, 330, 800
Negrello, M., Hopwood, R., Dye, S., et al. 2014, MNRAS, 440, 1999
Nguyen, H. T., Schulz, B., Levenson, L., et al. 2010, A&A, 518, L5
Ni, Q., Brandt, W. N., Yang, G., et al. 2021, MNRAS, 500, 4989
Oliver, S. J., Bock, J., Altieri, B., et al. 2012, MNRAS, 424, 1614
Oliver, S. J., Wang, L., Smith, A. J., et al. 2010, A&A, 518, L21
Oteo, I., Ivison, R. J., Dunne, L., et al. 2016, ApJ, 827, 34
Pantoni, L., Massardi, M., Lapi, A., et al. 2021, MNRAS, 507, 3998
Peebles, P. J. E. 1980, The Large-scale Structure of the Universe (Princeton, NJ: Princeton Univ. Press)
Peng, Y.-j., Lilly, S. J., Kovač, K., et al. 2010, ApJ, 721, 193
Pérez-Torres, M., Mattila, S., Alonso-Herrero, A., Aalto, S., & Efstathiou, A. 2021, A&ARv, 29, 2
Planck Collaboration VI 2020, A&A, 641, A6
Planck Collaboration XXVII 2015, A&A, 582, A30
Polletta, M. d., Wilkes, B. J., Siana, B., et al. 2006, ApJ, 642, 673
Pouliasis, E., Mountrichas, G., Georgantopoulos, I., et al. 2020, MNRAS, 495, 1853
Prandoni, I., Guglielmino, G., Morganti, R., et al. 2018, MNRAS, 481, 4548
Puccetti, S., Vignali, C., Cappelluti, N., et al. 2009, ApJS, 185, 586
Ranalli, P., Comastri, A., Vignali, C., et al. 2013, A&A, 555, A42
Reddy, N., Dickinson, M., Elbaz, D., et al. 2012, ApJ, 744, 154
Riechers, D. A., Bradford, C. M., Clements, D. L., et al. 2013, Natur, 496, 329
Rigopoulou, D., Kunze, D., Lutz, D., Genzel, R., & Moorwood, A. F. M. 2002, A&A, 389, 374
Robertson, B. E., Tacchella, S., Johnson, B. D., et al. 2023, NatAs, 7, 611
Rodighiero, G., Brusa, M., Daddi, E., et al. 2015, ApJL, 800, L10

Rujopakarn, W., Daddi, E., Rieke, G. H., et al. 2019, ApJ, 882, 107
Rujopakarn, W., Rieke, G. H., Eisenstein, D. J., & Juneau, S. 2011, ApJ, 726, 93
Sanders, D. B., Salvato, M., Aussel, H., et al. 2007, ApJS, 172, 86
Schlegel, D. J., Finkbeiner, D. P., & Davis, M. 1998, ApJ, 500, 525
Scholtz, J., Maiolino, R., D'Eugenio, F., et al. 2023, arXiv:2311.18731
Scoville, N., Aussel, H., Brusa, M., et al. 2007, ApJS, 172, 1
Sersic, J. L. 1968, Atlas de Galaxias Australes (Cordoba: Observatorio Astronomico)
Shankar, F., Bernardi, M., & Haiman, Z. 2009, ApJ, 694, 867
Shen, S., Mo, H. J., White, S. D. M., et al. 2003, MNRAS, 343, 978
Shen, X., Hopkins, P. F., Faucher-Giguère, C.-A., et al. 2020, MNRAS, 495, 3252
Shivaei, I., Alberts, S., Florian, M., et al. 2024, A&A, 690, A89
Shivaei, I., Reddy, N. A., Shapley, A. E., et al. 2017, ApJ, 837, 157
Silk, J., & Rees, M. J. 1998, A&A, 331, L1
Simpson, J. M., Smail, I., Swinbank, A. M., et al. 2015, ApJ, 807, 128
Simpson, J. M., Smail, I., Swinbank, A. M., et al. 2017, ApJ, 839, 58
Smith, J. D. T., Draine, B. T., Dale, D. A., et al. 2007, ApJ, 656, 770
Smolčić, V., Delvecchio, I., Zamorani, G., et al. 2017b, A&A, 602, A2
Smolčić, V., Novak, M., Bondi, M., et al. 2017a, A&A, 602, A1
Sommovigo, L., Ferrara, A., Pallottini, A., et al. 2022, MNRAS, 513, 3122
Spinoglio, L., Dasyra, K. M., Franceschini, A., et al. 2012, ApJ, 745, 171
Stanley, F., Harrison, C. M., Alexander, D. M., et al. 2015, MNRAS, 453, 591
Stefanon, M., Yan, H., Mobasher, B., et al. 2017, ApJS, 229, 32
Sturm, E., Lutz, D., Verma, A., et al. 2002, A&A, 393, 821
Suh, H., Civano, F., Hasinger, G., et al. 2019, ApJ, 872, 168
Symeonidis, M., Maddox, N., Jarvis, M. J., et al. 2022, MNRAS, 514, 4450
Symeonidis, M., Rigopoulou, D., Huang, J. S., et al. 2007, ApJL, 660, L73
Tadaki, K.-i., Belli, S., Burkert, A., et al. 2020, ApJ, 901, 74
Thorne, J. E., Robotham, A. S. G., Davies, L. J. M., et al. 2022, MNRAS, 509, 4940
Tommasin, S., Spinoglio, L., Malkan, M. A., & Fazio, G. 2010, ApJ, 709, 1257
Torbaniuk, O., Paolillo, M., Carrera, F., et al. 2021, MNRAS, 506, 2619
Treister, E., Urry, C. M., Chatzichristou, E., et al. 2004, ApJ, 616, 123
Treister, E., Urry, C. M., Van Duyne, J., et al. 2006, ApJ, 640, 603
Truebenbach, A. E., & Darling, J. 2017, MNRAS, 468, 196
van der Wel, A., Franx, M., van Dokkum, P. G., et al. 2014, ApJ, 788, 28
Vasudevan, R. V., & Fabian, A. C. 2007, MNRAS, 381, 1235
Venemans, B. P., Walter, F., Neeleman, M., et al. 2020, ApJ, 904, 130
Viero, M. P., Asboth, V., Roseboom, I. G., et al. 2014, ApJS, 210, 22
Vijayan, A., Kim, C.-G., Armillotta, L., Ostriker, E. C., & Li, M. 2020, ApJ, 894, 12
Ward, B. A., Eales, S. A., Pons, E., et al. 2022, MNRAS, 510, 2261
Weaver, J. R., Kauffmann, O. B., Ilbert, O., et al. 2022, ApJS, 258, 11
Weinberger, R., Springel, V., Hernquist, L., et al. 2017, MNRAS, 465, 3291
Weisskopf, M. C., Tananbaum, H. D., Van Speybroeck, L. P., & O'Dell, S. L. 2000, Proc. SPIE, 4012, 2
Werner, M. W., Roellig, T. L., Low, F. J., et al. 2004, ApJS, 154, 1
Wilkins, S. M., Vijayan, A. P., Lovell, C. C., et al. 2023, MNRAS, 518, 3935
Williams, R. E., Baum, S., Bergeron, L. E., et al. 2000, AJ, 120, 2735
Williams, R. E., Blacker, B., Dickinson, M., et al. 1996, AJ, 112, 1335
Wolfire, M. G., Vallini, L., & Chevance, M. 2022, ARA&A, 60, 247
Wright, E. L., Eisenhardt, P. R. M., Mainzer, A. K., et al. 2010, AJ, 140, 1868
Xue, Y. Q., Wang, S. X., Brandt, W. N., et al. 2012, ApJ, 758, 129
Yung, L. Y. A., Somerville, R. S., Finkelstein, S. L., et al. 2023, MNRAS, 519, 1578
Zavala, J. A., Casey, C. M., Manning, S. M., et al. 2021, ApJ, 909, 165
Zheng, Z., Berlind, A. A., Weinberg, D. H., et al. 2005, ApJ, 633, 791
Zubko, V., Dwek, E., & Arendt, R. G. 2004, ApJS, 152, 211